Dear Author

Please use this PDF proof to check the layout of your article. If you would like any changes to be made to the layout, you can leave instructions in the online proofing interface. Making your changes directly in the online proofing interface is the quickest, easiest way to correct and submit your proof. Please note that changes made to the article in the online proofing interface will be added to the article before publication, but are not reflected in this PDF proof.

If you would prefer to submit your corrections by annotating the PDF proof, please download and submit an annotatable PDF proof by clicking here and you'll be redirected to our PDF Proofing system.

Resource

Cell Metabolism

Single-Cell RNA Sequencing Maps Endothelial Metabolic Plasticity in Pathological Angiogenesis

Graphical Abstract

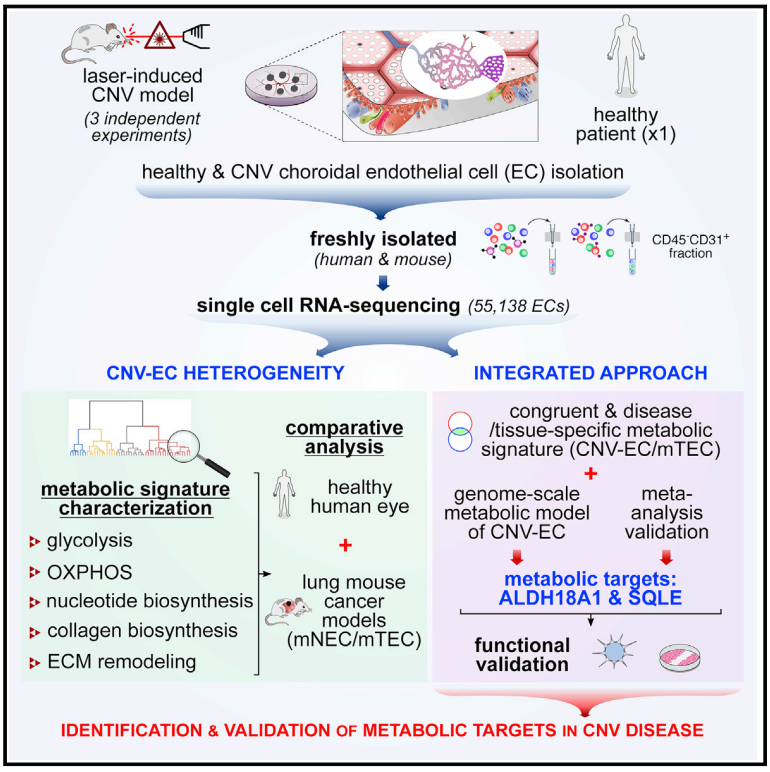

Highlights

- Single-cell RNA-seq reveals EC heterogeneity in choroidal neovascularization
- ECs display metabolic transcriptome heterogeneity in the cell cycle and quiescence
- Data integration with a genome scale metabolic model identifies angiogenic targets
- SQLE and ALDH18A1 are validated as metabolic angiogenic candidates

Authors

Katerina Rohlenova, Jermaine Goveia, Melissa García-Caballero, ..., Xuri Li, Yonglun Luo, Peter Carmeliet

Correspondence

lixr6@mail.sysu.edu.cn (X.L.), alun@biomed.au.dk (Y.L.), peter.carmeliet@kuleuven.vib.be (P.C.)

In Brief

Rohlenova et al. employ single-cell RNA sequencing to characterize angiogenic endothelial cells in murine choroidal neovascularization and compare the phenotypes to ECs in tumor angiogenesis. Using integrated analysis, genome-scale metabolic modeling, and *in vivo* methods, they identify and validate SQLE and ALDH18A1 as metabolic angiogenic candidates.

Data Resources

GSE77199

Rohlenova et al., 2020, Cell Metabolism *31*, 1–16
April 7, 2020
https://doi.org/10.1016/j.cmet.2020.03.009

CellPress

Please cite this article in press as: Rohlenova et al., Single-Cell RNA Sequencing Maps Endothelial Metabolic Plasticity in Pathological Angiogenesis, Cell Metabolism (2020), https://doi.org/10.1016/j.cmet.2020.03.009

Cell Metabolism
Resource

Single-Cell RNA Sequencing Maps Endothelial Metabolic Plasticity in Pathological Angiogenesis

Katerina Rohlenova,[1,19] Jermaine Goveia,[1,19] Melissa García-Caballero,[1,19] Abhishek Subramanian,[1,19] Joanna Kalucka,[1,16] Lucas Treps,[1] Kim D. Falkenberg,[1] Laura P.M.H. de Rooij,[1] Yingfeng Zheng,[2] Lin Lin,[3,4] Liliana Sokol,[1] Laure-Anne Teuwen,[1,5,6] Vincent Geldhof,[1] Federico Taverna,[1] Andreas Pircher,[1,14] Lena-Christin Conradi,[1,15] Shawez Khan,[1] Steve Stegen,[7] Dena Panovska,[8] Frederik De Smet,[8] Frank J.T. Staal,[9] Rene J. Mclaughlin,[9]

(Author list continued on next page)

[1]Laboratory of Angiogenesis and Vascular Metabolism, Center for Cancer Biology, VIB, Department of Oncology, Leuven Cancer Institute, KU Leuven, Leuven 3000, Belgium
[2]State Key Laboratory of Ophthalmology, Zhongshan Ophthalmic Center, Sun Yat-Sen University, Guangzhou 510060, Guangdong, PR China
[3]Department of Biomedicine, Aarhus University, Aarhus 8000, Denmark
[4]Lars Bolund Institute of Regenerative Medicine, BGI-Qingdao, Qingdao 266555, China
[5]Translational Cancer Research Unit, GZA Hospitals Sint-Augustinus, Antwerp 2610, Belgium
[6]Center for Oncological Research, University of Antwerp, Antwerp 2000, Belgium
[7]Laboratory of Clinical and Experimental Endocrinology, Department of Chronic Diseases, Metabolism and Aging, KU Leuven, Leuven 3000, Belgium
[8]Laboratory for Precision Cancer Medicine, Translational Cell & Tissue Research, Department of Imaging & Pathology, KU Leuven, Leuven 3000, Belgium
[9]Department of Immunology and Blood Transfusion, Leiden University Medical Center, Leiden 2300 RC, the Netherlands
[10]OXURION NV, Leuven 3001, Belgium
[11]BGI-Shenzhen, Shenzhen 518083, China

(Affiliations continued on next page)

SUMMARY

Endothelial cell (EC) metabolism is an emerging target for anti-angiogenic therapy in tumor angiogenesis and choroidal neovascularization (CNV), but little is known about individual EC metabolic transcriptomes. By single-cell RNA sequencing 28,337 murine choroidal ECs (CECs) and sprouting CNV-ECs, we constructed a taxonomy to characterize their heterogeneity. Comparison with murine lung tumor ECs (TECs) revealed congruent marker gene expression by distinct EC phenotypes across tissues and diseases, suggesting similar angiogenic mechanisms. Trajectory inference predicted that differentiation of venous to angiogenic ECs was accompanied by metabolic transcriptome plasticity. ECs displayed metabolic transcriptome heterogeneity during cell-cycle progression and in quiescence. Hypothesizing that conserved genes are important, we used an integrated analysis, based on congruent transcriptome analysis, CEC-tailored genome-scale metabolic modeling, and gene expression meta-analysis in cross-species datasets, followed by *in vitro* and *in vivo* validation, to identify SQLE and ALDH18A1 as previously unknown metabolic angiogenic targets. Q2

INTRODUCTION Q3 Q4 Q5

Endothelial cell (EC) metabolism regulates angiogenesis, and is an emerging target for anti-angiogenic therapy (AAT) in cancer and wet age-related macular degeneration (AMD) (Eelen et al., 2018). The design of new AATs by targeting EC metabolism would benefit from a better understanding of individual EC

Context and Significance

Targeting the metabolism of endothelial cells (ECs) is a promising strategy to block pathological blood vessel growth, or angiogenesis, for the treatment of diseases like cancer. Understanding the landscape of metabolic gene expression at the single-cell level will aid in identifying novel angiogenic targets. Here, researchers in Belgium and their colleagues surveyed thousands of ECs in pre-clinical models of age-related macular degeneration and lung cancer. Their comprehensive investigation identified genes and metabolic pathways that are congruently upregulated across diseases and tissues during angiogenesis. Using an integrated analysis, the researchers generated a list of prioritized metabolic candidates and validated the importance of two candidates, SQLE and ALDH18A1, in pathological angiogenesis, supporting their potential as therapeutic targets.

Please cite this article in press as: Rohlenova et al., Single-Cell RNA Sequencing Maps Endothelial Metabolic Plasticity in Pathological Angiogenesis, Cell Metabolism (2020), https://doi.org/10.1016/j.cmet.2020.03.009

Stefan Vinckier,[1] Tine Van Bergen,[10] Nadine Ectors,[8] Patrik De Haes,[10] Jian Wang,[11,12] Lars Bolund,[3,4] Luc Schoonjans,[1,2] Tobias K. Karakach,[1,17,18] Huanming Yang,[11,12] Geert Carmeliet,[7] Yizhi Liu,[2] Bernard Thienpont,[13] Mieke Dewerchin,[1] Guy Eelen,[1] Xuri Li,[2,20,*] Yonglun Luo,[3,4,11,12,20,*] and Peter Carmeliet[1,2,20,21,*]

[12]China National GeneBank, BGI-Shenzhen, Shenzhen 518120, China
[13]Laboratory for Functional Epigenetics, Department of Human Genetics, KU Leuven, Leuven 3000, Belgium
[14]Present address: Department of Hematology and Oncology, Internal Medicine V, Medical University Innsbruck, Innsbruck, Austria
[15]Present address: Clinic of General, Visceral and Pediatric Surgery, University Medical Center Göttingen, Göttingen, Germany
[16]Present address: Aarhus Institute of Advanced Studies (AIAS), Department of Biomedicine, Aarhus University, Aarhus DK-8000, Denmark
[17]Present address: Bioinformatics Core Laboratory, Children's Hospital Research Institute of Manitoba, Winnipeg, MB, Canada
[18]Present address: Rady Faculty of Health Sciences, Department of Pediatrics and Child Health, University of Manitoba, Winnipeg, MB, Canada
[19]These authors contributed equally
[20]Senior author
[21]Lead Contact
*Correspondence: lixr6@mail.sysu.edu.cn (X.L.), alun@biomed.au.dk (Y.L.), peter.carmeliet@kuleuven.vib.be (P.C.)
https://doi.org/10.1016/j.cmet.2020.03.009

metabolism, but it remains unknown if ECs express a heterogeneous metabolic gene signature and how single ECs reprogram their metabolic transcriptome signature when forming new vessels in disease. However, metabolomics (measuring metabolite levels or metabolic fluxes) is insufficiently sensitive to determine single EC metabolism. Since we documented that changes in metabolic gene expression signatures at the bulk population level can be predictive of changes in metabolism in ECs (Bruning et al., 2018; Cantelmo et al., 2016; Kalucka et al., 2018; Vandekeere et al., 2018), we analyzed the metabolic transcriptome of ECs at the single-cell level.

During vessel sprouting, a navigating tip EC leads the way, while proliferating stalk cells elongate the vessel sprout (Potente et al., 2011); once newly formed vessels become perfused, ECs adopt a quiescent phalanx phenotype (Welti et al., 2013). ECs rely on metabolic reprogramming when switching from quiescence to vessel sprouting (Eelen et al., 2018; Li et al., 2019; Sawada and Arany, 2017; Yu et al., 2018). In tumors, bulk metabolic gene expression profiling identified metabolic targets in tumor ECs (Cantelmo et al., 2016). AMD is a common blinding disease of elderly people, characterized by ocular neovascularization. Laser-induced choroid neovascularization (CNV) is a preclinical model of AMD (Ambati and Fowler, 2012). Since angiogenic ECs in AMD/CNV have not been studied at the single-cell level, we used single-cell RNA sequencing (scRNA-seq) to profile their (metabolic) transcriptome heterogeneity.

Anti-VEGF drugs are used for the treatment of cancer and AMD, but resistance limits their efficacy (Jain, 2014; Yang et al., 2016). Hence, there is an unmet clinical need to identify novel angiogenic targets. scRNA-seq is a powerful technology to identify such candidates, but an outstanding challenge is to prioritize targets for further clinical translation. Here, we present a strategy, starting from scRNA-seq and complemented with orthogonal techniques, to prioritize metabolic targets that control angiogenesis.

RESULTS

Identification and Characterization of CNV-ECs by scRNA-Seq

To model CNV in mice, we laser-induced 10 lesions per eye and microdissected choroids 7 days later. We pooled choroids from 6 mice and repeated this procedure 3 times, using choroids from healthy mice as controls (6 mice per sample, in triplicate) (Figures 1A and 1B). For comparative analysis, we generated a pooled sample of two choroids from one healthy human donor (see below). Single-cell suspensions were MACS-enriched for $CD45^{-}/CD31^{+}$ ECs (Cantelmo et al., 2016) and subjected to scRNA-seq. After quality filtering (Table S1), batch correction, and *in silico* EC selection, graph-based clustering was performed to group a total of 28,337 ECs according to their gene expression profile. Clusters were annotated based on marker genes (Tables S2 and S3) and results were visualized using t-distributed stochastic neighbor embedding (t-SNE) (Figures 1C, 1D, S1A, and S1B).

CECs from control mice were indistinguishable from healthy peripheral CECs from lasered mice and clustered together (Figures 1C–1F). We detected a new separate population in lasered mice, not present in healthy CECs, representing CNV-ECs (Figure 1D). Compared to healthy CECs, CNV-ECs expressed activation markers associated with response to injury such as *Sparc* (Bradshaw and Sage, 2001) and *Col18a1*, a source of the angiostatic endostatin, previously used for CNV treatment (Marneros et al., 2007), a finding confirmed at the protein level by quantitative mass cytometry (CyTOF) (Figures 1G, S1C, and S1D; Table S2).

Taxonomy of CECs and CNV-ECs

In CECs, we identified previously unknown sublineages of the classical arterial, capillary, and venous EC phenotypes (Figures 1E–1G; for more complete description of marker genes and putative inferred biological activity, see Table S3). For instance, we identified large supply arteries (P1 on Figure 1D), smaller ramifying arterioles (P2) and arterial ECs expressing the shear stress marker (*Pi16*) (tentatively coined shear-stress induced arterial ECs [P3]), and a laser-induced arterial subpopulation (activated arterial CEC) that upregulated activation markers and matricellular proteins (P4) (Figure 1H). Activated arterial CECs clustered together with other arterial phenotypes (Figure 1D), suggesting a relatively normal transcriptome. Capillary CEC phenotypes expressed signatures of the outer (P5) and inner choriocapillaries (P6), characterized by the differential expression of genes involved in fenestration and VEGF signaling (Blaauwgeers et al., 1999; McLeod et al., 1995) (Table S2). Venous subclusters included cells expressing markers of large caliber vessels (P7), venules (P8), shear stress

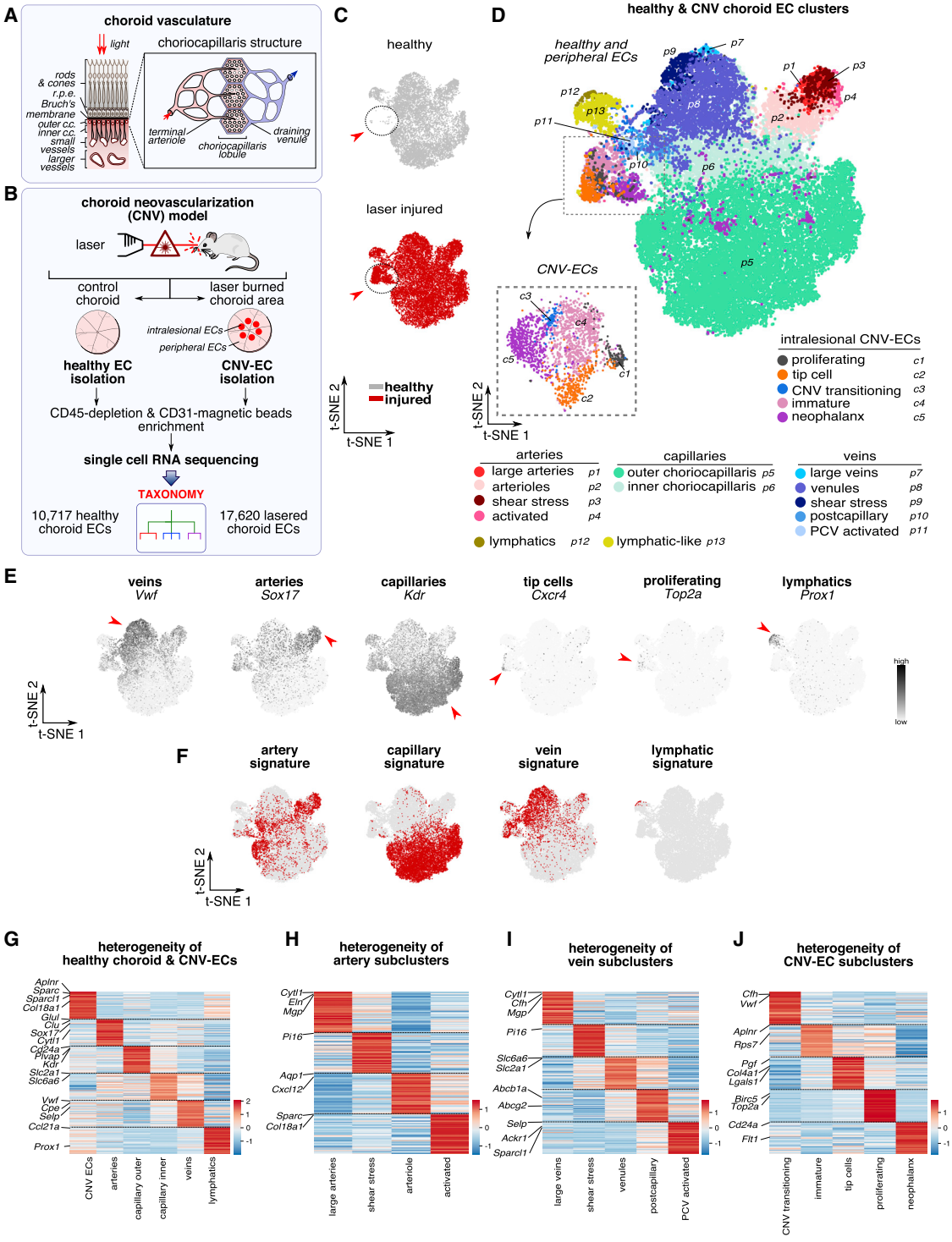

Figure 1. Heterogeneity of Choroid NEC and CNV-EC Phenotypes

(A) Schematic overview of the choroidal vasculature.

(B) Schematic overview of the study design.

(C) t-SNE plot, color-coded for the sample type. ECs isolated from healthy choroid are depicted in gray (top); ECs isolated from laser-injured choroids in red (bottom). Red arrowhead and dotted circles indicate an emerging population of laser-injured specific CNV-EC phenotypes.

(D) t-SNE visualization of EC subpopulations in healthy and laser-injured choroids. CNV-EC phenotypes (red arrowhead in C) are boxed in the global t-SNE plot and shown in a separate t-SNE plot on the lower left. Subclusters of peripheral (p) and intralesional CNV-ECs (c) are numbered.

(legend continued on next page)

(P9), post-capillary venules (pcvs) (P10) that upregulated a previously identified CEC signature of resident endothelial stem cells (ESCs) (Naito et al., 2012; Wakabayashi et al., 2013), and an activated pcv CEC phenotype (p11) (Figures 1I and S1E). We observed two putative lymphatic EC phenotypes (LEC [P12] and LEC-like [P13]) that differentially expressed *Lyve-1* (Figure 1D; Table S2). The existence of lymphatics in the choroid remains debated (Heindl et al., 2015; Koina et al., 2015).

Angiogenic CNV-ECs were distinct from normal CECs and included proliferating ECs (C1 in Figure 1D) and tip ECs (C2), but also 3 previously unknown phenotypes that expressed signatures associated with transitioning from pcv to angiogenic EC phenotypes (transitioning CNV-ECs [C3]), and immature (immature [C4]) and maturing (neophalanx [C5]) neovasculature (Figure 1J). Tip cells upregulated transcripts of the disease-restricted angiogenic factor *Pgf* (encoding placental growth factor, Plgf) (Figures 1J and S1F). Immature ECs were characterized by the lack of specific marker gene expression, but expressed activation markers and upregulated ribosomal gene expression consistent with an activated intermediate phenotype. Neophalanx ECs expressed markers of mature capillaries and arteries, and were characterized by upregulation of a Notch signaling gene signature (Figure S1G).

Interestingly, transcription factor activity analysis using single-cell regulatory network inference and clustering (SCENIC) (Aibar et al., 2017) indicated differential transcription factor activity in EC subtypes (Figure 2A). Consistent with previous reports, *Nr2f2* expression was induced in activated pcvs and transitioning ECs (Jeong et al., 2017), while *Sox17* expression was highest in arterial ECs (Corada et al., 2013; You et al., 2005). SCENIC analysis of CNV-ECs also identified transcription factors not previously implicated in EC specification, such as in tip (*Tgif1*), immature (*Smad1* and *Sox4*), and proliferating (*Trp53*) CNV-ECs (Figure 2A).

We validated the taxonomy using orthogonal *in situ* localization techniques. Quantitative RNAscope to count transcript numbers, combined with staining for the EC marker CD105, confirmed that arterial (*Gja4*) and venous (*Nr2f2*) marker transcripts did not colocalize in the same CNV-ECs (Figure S1H). We confirmed by immunostaining of healthy choroids the expression of the following EC markers: (1) artery ECs (ELN) and arteriole ECs (CXCL12) (Figures S2A–S2C), (2) capillary ECs (VEGFR2) (Figure S2D), and (3) venous ECs (VWF and SELP) (Figures S2E and S2F). Immunostaining of CNV lesions confirmed the expression of a marker of immature ECs (APLNR), tip ECs (PlGF, LXN, and CXCR4), and pcv ECs (SPARCL1) (Figures S2G–S2J).

Metabolic Transcriptome Reprogramming during Pathological Vessel Sprouting

We explored if ECs underwent a differentiation trajectory during vessel sprouting and if EC differentiation was associated with metabolic transcriptome changes. Trajectory inference analysis predicted that the hierarchy of angiogenic phenotypes resulted from differentiation of activated pcv CECs to transitioning CNV-ECs, then to immature CNV-ECs, which thereafter differentiated to tip cells and finally to more mature neophalanx CNV-ECs (Figure 2B). This prediction extends previous morphological evidence that neovessels may originate from pcvs (Folkman, 1982). Since pcv CECs expressed a previously validated signature of resident ESCs, our analysis provides further suggestion that ESCs might contribute to new vessel sprouting, as previously established by lineage tracing (Corey et al., 2016; Manavski et al., 2018; McDonald et al., 2018; Mondor et al., 2016; Red-Horse et al., 2010; Wakabayashi et al., 2013, 2018).

Interestingly, when focusing on metabolic genes and pathways, we noted that membrane transport, ATP synthase, and glycolysis gene signatures were dynamically regulated during differentiation from quiescent vein to angiogenic ECs (Figure 2B). Maximal differences in metabolic gene expression of central carbon metabolism were observed in the most angiogenic EC phenotypes (immature and tip ECs), possibly suggesting that these ECs had higher metabolic demands to execute their biological functions (Figure 2B).

Congruency Analysis of Metabolic Transcriptome Reprogramming

We explored whether metabolic transcriptome reprogramming was specific to CNV-ECs or a more general hallmark of the angiogenic switch in pathological angiogenesis (such as in tumors), as this would address a fundamental question in vascular biology of whether vessels in different tissues and diseases form via similar or different mechanisms. We therefore explored to which extent CNV and tumors contained similar EC phenotypes, and whether they expressed congruent genes.

Similarity and Congruency Analysis

We analyzed a publicly available, previously in-house generated dataset of murine lung tumor ECs (TECs) (Goveia et al., 2020), which comprised largely similar EC phenotypes as CNV-ECs. However, in addition, murine lung TECs contained breach and pre-breach ECs (that expressed both tip cell and podosome rosette markers, presumably involved in vessel sprouting initiation), and interferon ECs (displaying a transcriptome response to interferon, possibly involved in immune surveillance) (Goveia et al., 2020). Focusing on all detected genes, we explored whether similar EC phenotypes could be detected in these diseases, and whether they expressed congruent genes.

We performed differential gene expression and gene set enrichment analysis to determine which processes were upregulated in CNV-ECs and TECs versus CECs and NECs, respectively (Figures 2C and 2D). Gene sets associated with proliferation, hypoxia signaling, and extracellular matrix formation were commonly upregulated (Figure 2C). Consistently, many of the 175 commonly upregulated genes were involved in extracellular

(E and F) t-SNE plots, color-coded for the expression of the indicated marker genes (E) or gene sets (F). Red arrowheads indicate cells with high expression of the indicated marker gene. Scale: white/gray is low expression; black (gene) or red (gene sets) is high gene expression.

(G–J) Heatmap of gene expression levels of the top 50 marker genes for broad categories of EC phenotypes (G), artery subclusters (H), vein subclusters (I), and CNV-EC subclusters (J). In this and all further heatmaps depicting marker genes, colors represent row-wise scaled gene expression with a mean of 0 and SD of 1 (*Z* scores).

c.c., choriocapillaris; r.p.e., retinal pigment epithelium. See also Figures S1 and S2 and Tables S1, S2, and S3.

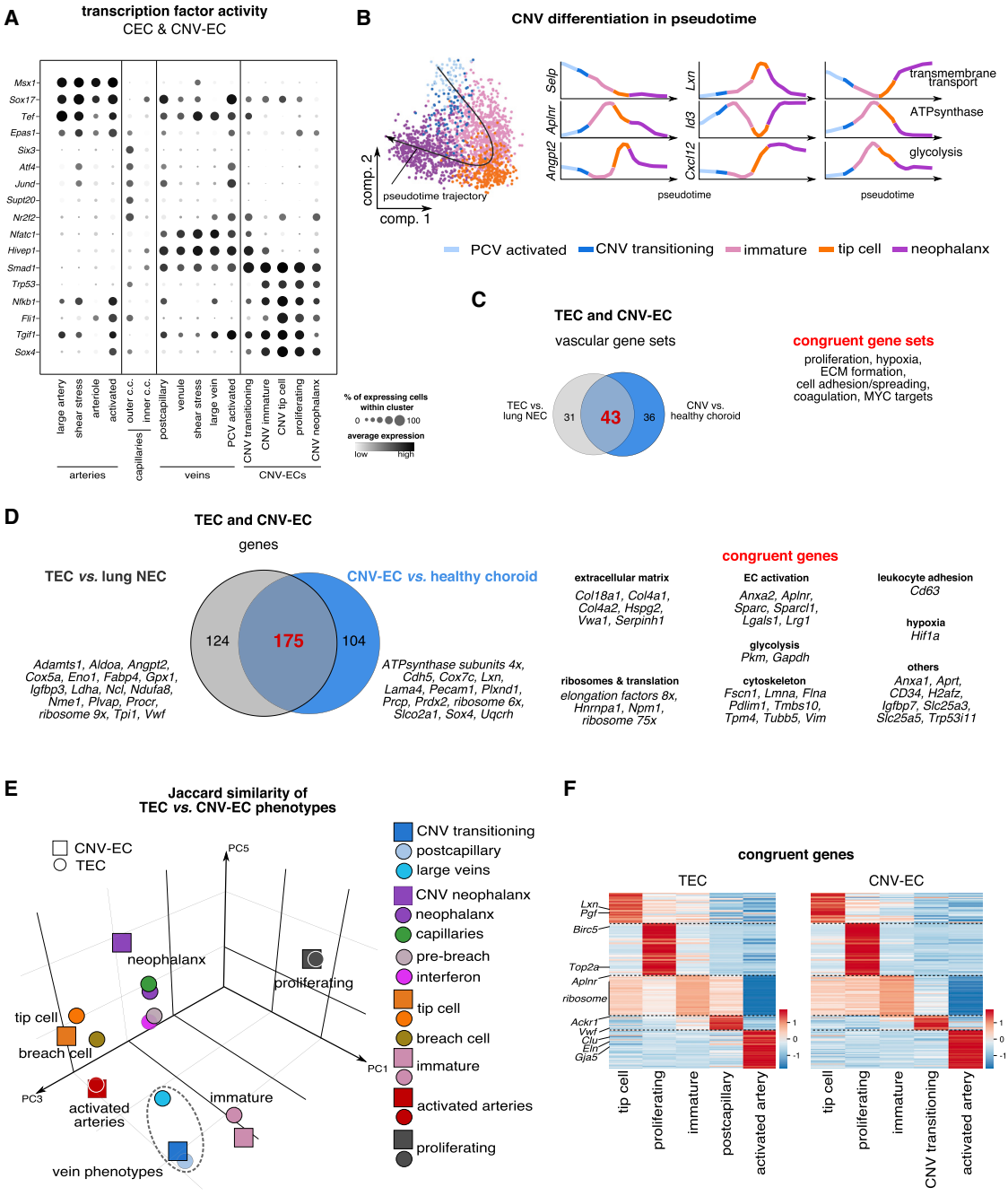

Figure 2. Gene Expression Signatures in CNV and TEC Subtypes

(A) Dot plot heatmap of the inferred activity of the indicated transcription factors. Scale: white/gray is low expression; black is high gene expression; dot size corresponds to the fraction of cells in each cluster that have higher than average activity of the indicated transcription factor.

(B) Pseudotime trajectory of the indicated CNV-EC phenotypes (left) and Loess regression-smoothened gene expression of the indicated genes and metabolic gene sets in pseudotime (right).

(C) Vascular gene sets upregulated in TECs (versus lung NECs) and in CNV ECs (versus choroid CECs). Gene sets congruently upregulated in TECs and CNV-ECs are summarized on the right.

(D) Genes upregulated in TECs versus NECs and choroid CECs versus CNV-ECs. A selection of genes upregulated in lung TECs versus NECs (left) and in CNV-ECs versus choroid CECs (right) are listed. Genes congruently upregulated in TECs and CNV-ECs are listed on the right. Genes encoding ribosomal proteins are not listed individually; instead, their total number is displayed.

(legend continued on next page)

matrix remodeling, cytoskeleton, glycolysis, EC activation, and others. Interestingly, Aplnr, an angiogenic and vasculoprotective gene that regulates EC metabolism (Apostolidis et al., 2018; Hwangbo et al., 2017), was identified as a congruent marker of CNV-ECs and TECs (Figure 2D).

Since differential analysis of pooled populations may not adequately discover genes with restricted expression in small EC subpopulations such as tip and proliferating cells, we determined whether the same EC subpopulations were present in CNV-ECs and TECs. We used the Jaccard similarity index to score the similarity of marker gene sets of all EC subpopulations, and observed that marker gene sets across CNV-ECs and TECs were relatively similar for several EC subpopulations (Figures 2E and S3A). Further, TECs and CNV-ECs of the same phenotype expressed congruent marker genes (Figure 2F). Similar to CNV-ECs, trajectory inference analysis predicted that the hierarchy of TEC phenotypes originated in veins expressing resident ESC markers (Goveia et al., 2020; Wakabayashi et al., 2018) to postcapillary veins and further to an immature TEC phenotype, tip cells, neophalanx TECs, and activated arteries (Figure S3B).

Metabolic Transcriptome Signatures

Focusing on metabolic genes, we observed that proliferating ECs in both disease models upregulated the expression of metabolic genes involved in one-carbon metabolism, nucleotide synthesis, tricarboxylic acid (TCA) cycle, and oxidative phosphorylation (OXPHOS) (Figure 3A). In contrast, glycolytic gene expression was upregulated in proliferating, tip, and immature ECs in tumors, and was elevated in CNV in proliferating ECs, but less in tip and immature ECs (Figure 3B). These observations might suggest that the metabolic demands of proliferating ECs are disease- or tissue-type independent, while metabolic adaptations of other subtypes may be more plastic.

The metabolic gene expression signatures between the different TEC phenotypes were more outspoken, possibly reflecting the harsh nutrient-deprived micro-environment in tumors and the fact that TECs grow in an uncontrolled, non-resolving manner. Indeed, heatmap analysis revealed that most TECs exhibited a different metabolic transcriptome signature (Figure S3C). Subsequent analysis at the gene level showed that capillary TECs upregulated the expression of genes controlling lipid uptake (Figures 3C and S3C), raising the question of whether they need lipids for internal use when switching to quiescence (Kalucka et al., 2018) and/or for trans-EC transport to cancer cells for energy production or lipogenesis (Santos and Schulze, 2012). Venous TECs upregulated transcripts of genes involved in prostaglandin metabolism (Figures 3C and S3C), suggesting a role in vasoregulation, sprouting, or vascular inflammation (Félétou et al., 2011; Iñiguez et al., 2003). Interferon (IFN)-activated TECs upregulated genes involved in nucleotide catabolism to salvage/lower nucleotide content (Figure 3C) (Barankiewicz et al., 1986). In turn, breach TECs upregulated genes involved in extracellular matrix production the most, in line with their presumed role in vessel sprouting initiation (Goveia et al., 2020) (Figures 3C and S3C).

Correlation with Transcription Factor Expression

Consistent with literature reports (Kanda et al., 2009), correlating the gene signatures with inferred transcription factor activity scores revealed that Pparg correlated with the induction of a triglyceride catabolism signature. Interestingly, hypoxia, as indicated by the inferred activity of HIF-1α, correlated with glycolysis and OXPHOS gene expression in TECs (Figure S3D). While expected for glycolysis (given that hypoxia upregulates glycolysis; Eales et al., 2016), the upregulation of OXPHOS genes in hypoxic conditions was surprising (given that hypoxia suppresses OXPHOS; Eales et al., 2016; Semenza, 2011), but in line with findings that HIF-1α activation can occur at oxygen levels that are not sufficiently low to suppress mitochondrial respiration (Eales et al., 2016). Thus, while proliferating CNV-ECs and TECs upregulate OXPHOS and glycolysis gene signatures, the metabolic transcriptome profile of other angiogenic ECs is rather diverse across diseases.

Analysis of Metabolic Transcriptome Reprogramming during the Cell Cycle

Since our congruency analysis showed that proliferating CNV-ECs and TECs have similar gene expression profiles, we analyzed their (metabolic) signature and transcription factor regulation in more detail. We therefore developed a prediction model to reconstruct continuous cell-cycle pseudotime in proliferating murine CNV-ECs and TECs based on periodically expressed genes identified in cultured TECs (Figures S3E–S3I; STAR Methods). Comparative analysis of the top 1% most periodic genes in proliferating TECs and CNV-ECs revealed 97 genes that were periodically expressed during the cell cycle in both models, 43 of which were not previously described in reference databases (Santos et al., 2015). Interestingly, in both models, several metabolic genes ranked in the top 1% most periodic genes (*Rrm2*, *Tk1*, *Tyms*, *Dut*, *Rrm1*, and *Dctpp1*) (Figure 3D; Table S4). Further, gene set variation analysis revealed that various metabolic pathways involved in nucleotide biosynthesis (e.g., one-carbon metabolism and pyrimidine nucleoside biosynthesis) ranked among the top 5% most periodically expressed gene sets (Figure 3E; Table S4). Overall, our scRNA-seq offers new possibilities to study metabolic gene expression kinetics during the cell cycle.

Metabolic Angiogenic Target Identification

Identification of Commonly Upregulated Metabolic Genes

Since OXPHOS and glycolysis are validated metabolic angiogenic targets (Cantelmo et al., 2016; De Bock et al., 2013; Diebold et al., 2019), we designed an integrated analysis to identify other previously unrecognized angiogenic candidates regulating EC metabolism. We thus performed differential gene expression analysis to determine which metabolic genes and gene sets were commonly upregulated in TECs and CNV-ECs, versus normal ECs. Pathway mapping of gene transcripts involved in central

(E) Three-dimensional principal component analysis (PCA) on the pairwise Jaccard similarity coefficients of marker gene sets between subpopulations in TECs and CNV-ECs. Squares denote CNV-EC phenotypes; circles denote TEC phenotypes. Note that equivalents of breach, pre-breach, and interferon TEC phenotypes were not present in CNV-ECs.

(F) Heatmap of expression levels of congruent genes in TEC and CNV-EC phenotypes (all genes analyzed). Note that the TEC and CNV-EC heatmaps show the same set of congruent genes.

Comp, component; PC, principal component. See also Figure S3.

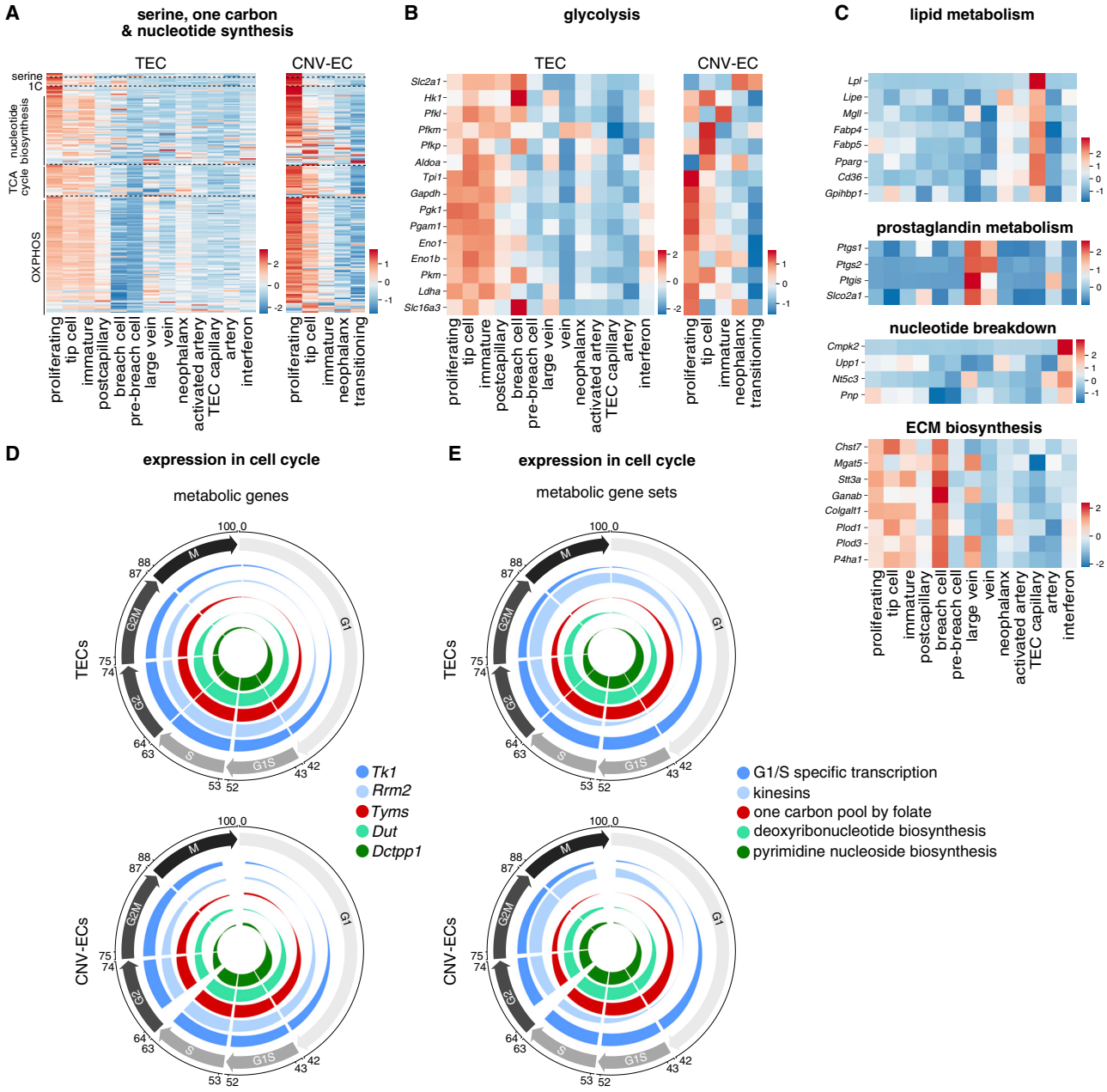

Figure 3. Metabolic Heterogeneity in TECs and CNV-ECs

(A) Heatmap of the gene expression levels of the indicated metabolic pathways in TEC and CNV-EC subpopulations. Genes were grouped according to metabolic pathways and ordered so that the most discriminative genes for proliferating ECs are depicted first.

(B) Heatmap of gene expression levels of the indicated glycolytic genes in TEC and CNV-EC subpopulations.

(C) Heatmap of gene expression levels of the indicated genes in TECs.

(D and E) Circos plot representation of Loess regression-smoothened gene expression of the indicated genes (D) and gene sets (E) during the cell cycle in TECs (top) and CNV-ECs (bottom). Cell-cycle phase assignment, indicated as color-coded sectors, was based on the known periodicity of cyclins. Cell-cycle pseudotime is represented as a percentage and indicated outside of the circos plot, starting (t = 0%) from cytokinesis (start of G1). The thickness of the line corresponds to the expression levels.

See also Figure S3 and Table S4.

carbon metabolism confirmed that CNV-ECs upregulated transcripts of metabolic pathways supporting biomass synthesis, including glycolysis, nucleotide synthesis, TCA cycle, OXPHOS, and others (Figures 4A and 4B). Several of these pathways are also involved in other metabolic/biological activities, such as redox and energy homeostasis (Eelen et al., 2018). Compared to NECs, TECs showed a qualitatively largely similar upregulation of anabolic pathways (Figures 4A and S4A).

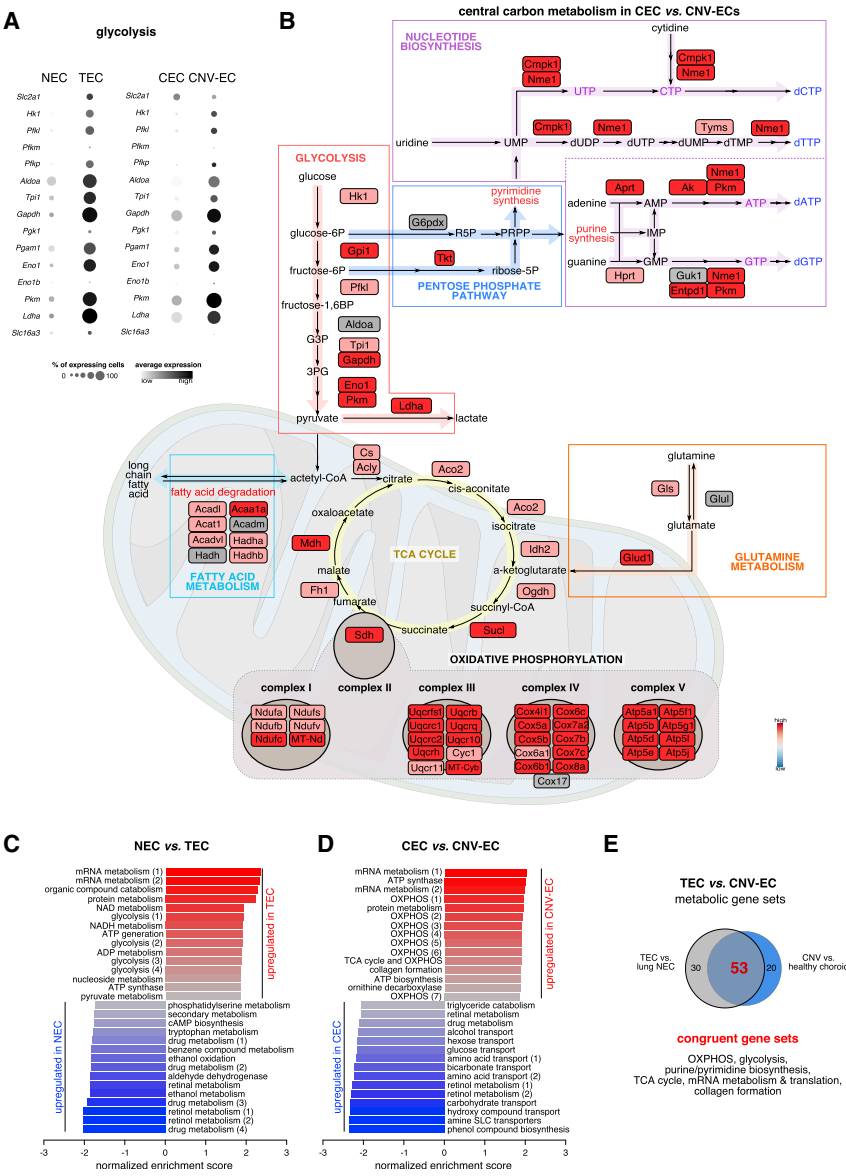

Figure 4. Global Metabolic Reprogramming in Pathological Angiogenesis

(A) Dot plot heatmap of the indicated glycolytic genes. The dot size corresponds to the fraction of cells that have higher than average activity of the indicated genes. Scale: white/gray is low expression; black is high gene expression.

(B) Map of upregulated central carbon metabolic pathways in CNV-ECs versus peripheral CECs. Blue color indicates downregulated expression, red upregulated expression, and gray unchanged expression.

(C and D) Metabolic gene set enrichment analysis in NEC versus TECs (C) and CEC versus CNV-ECs (D) ($q < 0.25$ for all gene sets). Numbers between parentheses indicate alternative gene sets pertaining to the same biological function or signaling pathway.

(E) Metabolic gene sets, upregulated in TECs (versus lung NECs) and in CNV-ECs (versus choroid CECs). Congruent upregulated metabolic pathways are listed underneath.

See also Figure S4.

The upregulation of OXPHOS and TCA cycle gene expression signatures in proliferating ECs was noteworthy, when considering that ECs are glycolysis-addicted (Cantelmo et al., 2016; De Bock et al., 2013), but is in line with reports showing the importance of OXPHOS for EC proliferation (Diebold et al., 2019; Ying et al., 2017). The upregulation of a glycolysis transcriptome signature in TECs has been validated by functional evidence that genetic deletion in ECs or pharmacological blockade of the glycolytic activator PFKFB3 reduces TEC proliferation and induces tumor vessel normalization (Cantelmo et al., 2016), and may also explain why treatment with a PFKFB3 blocker inhibited CNV in the mouse (Schoors et al., 2014).

An unbiased metabolic gene set enrichment analysis, combined with a congruency analysis to identify commonly upregulated metabolic pathways, revealed that genes involved in pathways in central carbon metabolism were among the most upregulated in TECs and CNV-ECs, including glycolysis, OXPHOS, nucleotide biosynthesis, and TCA cycle, compared to NECs and peripheral ECs (Figures 4C–4E). Notably, transcripts of genes involved in collagen synthesis were also highly upregulated in angiogenic ECs in both diseases (Figure 4E). Thus, based on transcriptome analysis, angiogenic ECs have at least two prominent metabolic gene expression signatures, i.e., that of biomass production for proliferation and of collagen biosynthesis for extracellular matrix remodeling.

Prediction of Candidates with Functionally Relevant Role in Metabolism by GEMs

Given that changes in transcript levels of metabolic genes alone may not relate to changes in metabolic fluxes, we used genome-scale metabolic models (GEMs) to *in silico* prioritize metabolic candidates. GEMs are mathematical representations of a network of active metabolic enzymes (pathways) (Kim and Lun, 2014; Ryu et al., 2015) and represent computational tools to predict the importance of metabolic reactions for biological responses (Pagliarini et al., 2016; Thiele and Palsson, 2010). We constructed a CEC-tailored GEM based on the generic human metabolic reconstruction RECON1 and scRNA-seq data from 1,670 freshly isolated human CECs, which recapitulated murine CEC phenotypes but with lower resolution (Figures 5A, S4B, and S4C), and optimized it for biomass (as a proxy for proliferation) or collagen production using two distinct EC-specific objective functions.

Using the CEC-tailored GEM, we identified 288 essential genes for biomass synthesis (Table S5), involved in glycolysis, TCA cycle, pentose phosphate pathway, OXPHOS, fatty acid oxidation, nucleotide synthesis and salvage, cholesterol biosynthesis, sphingolipid metabolism, and amino acid metabolism

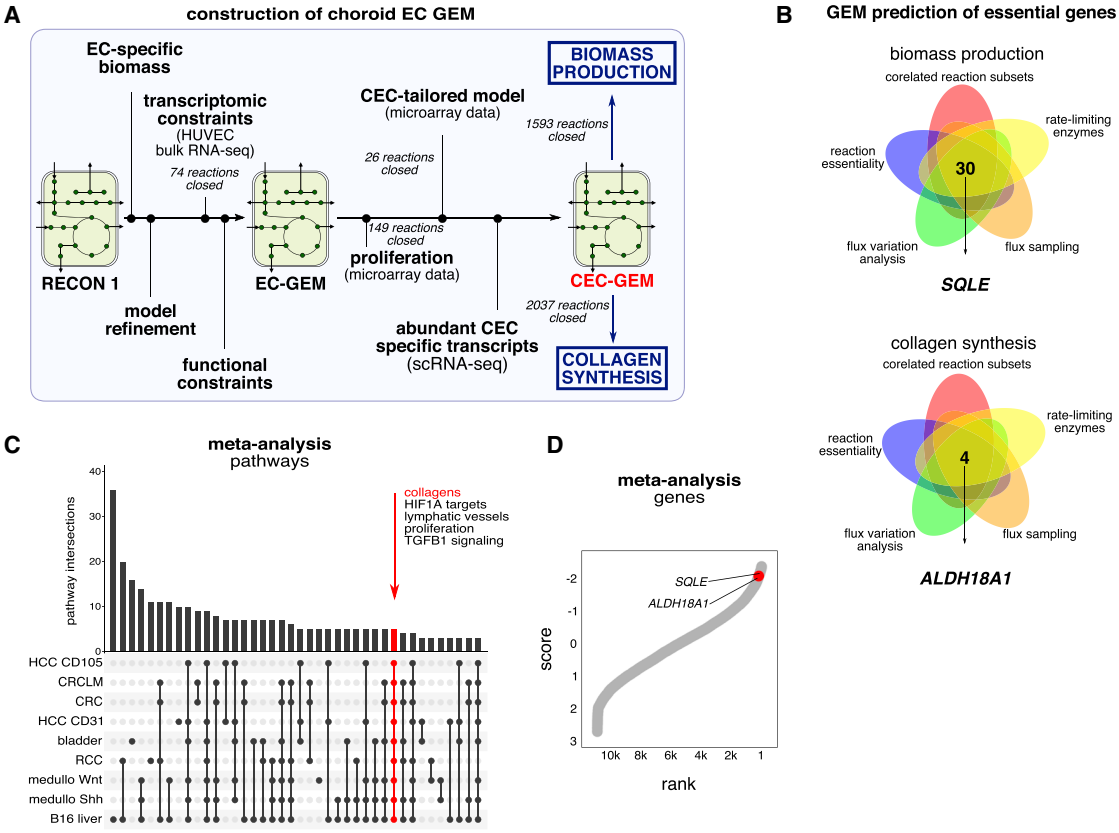

Figure 5. Metabolic Target Prediction

(A) Schematic representation of GEM reconstruction.

(B) Venn diagrams indicating metabolic genes that encode rate-limiting enzymes and are predicted to be essential for biomass production (top) and collagen biosynthesis (bottom) by four different methods (see STAR Methods for details).

(C) Upset plot visualization of the results of a differential gene set variation enrichment meta-analysis of nine bulk transcriptomics datasets, showing the number of genes that were more highly expressed in TECs than NECs isolated from the indicated tumor type. The bar graph represents the number of gene sets detected in the tumor type(s) indicated by the dot plot panel below. Five gene sets (displayed on the figure; involved in the displayed processes) were consistently higher expressed in TECs than NECs (red bar graph and intersection). HCC, hepatocellular carcinoma; CRCLM, colorectal cancer liver metastasis; CRC, colorectal cancer; medullo Wnt, Wnt-driven medulloblastoma; medullo Shh, sonic hedgehog driven medulloblastoma; RCC, renal cell carcinoma.

(D) Gene expression meta-analysis of the nine NEC versus TEC datasets shown in (C). The S-curve has 10,850 dots, representing genes that were detected in all nine datasets. x axis, rank numbers from 1 to 10,850 (consistently overexpressed genes in TECs have a low rank number; consistently downregulated genes have a high rank number); y axis, the scaled meta-analysis score (consistently overexpressed genes in TECs have a low meta-analysis score; consistently down-regulated genes have a high meta-analysis score). SQLE and ALDH18A1 are shown as red dots and listed on the left.

See also Figure S5 and Table S5.

(Table S5). The roles of glycolysis (De Bock et al., 2013), OXPHOS (Diebold et al., 2019), fatty acid oxidation (Schoors et al., 2015), serine metabolism (Vandekeere et al., 2018), and glutamine metabolism (Huang et al., 2017) in biomass synthesis and EC proliferation have been established, thus validating the predictive potential of the CEC-tailored GEM. However, a possible role of cholesterol synthesis in EC growth has only minimally been studied, without conclusive results. Further, consistent with previous reports (Phang, 2019), the CEC-tailored GEM predicted the essentiality of proline biosynthesis for collagen production. In addition, glutamine and glutamate transporters, and enzymes involved in alanine, glycine, and serine metabolism, were also predicted to be essential, reflecting that the molecular composition of collagen consists of >70% of (hydroxy)proline, glycine, glutamate, and alanine (Eastoe, 1955).

Integrated Analysis to Prioritize Metabolic Genes for Functional Validation

To identify functionally relevant metabolic angiogenic targets in CNV-ECs, we performed an integrated analysis (Figure S5A). Specifically, we focused on the subset of rate-limiting single gene encoded metabolic enzymes, predicted by GEM to be essential for biomass production or collagen biosynthesis (Figure 5B; Table S5). We selected candidates that were more highly expressed in CNV-ECs than CECs, yielding 30 genes for biomass production and 4 for collagen synthesis (Table S5). Second, we reasoned that genes that were conserved across models, diseases, and species represent robust targets. We thus filtered for genes consistently upregulated also in tumor angiogenesis, resulting in a set of 17 candidate genes. Finally, unbiased meta-analysis across 9 different murine and human

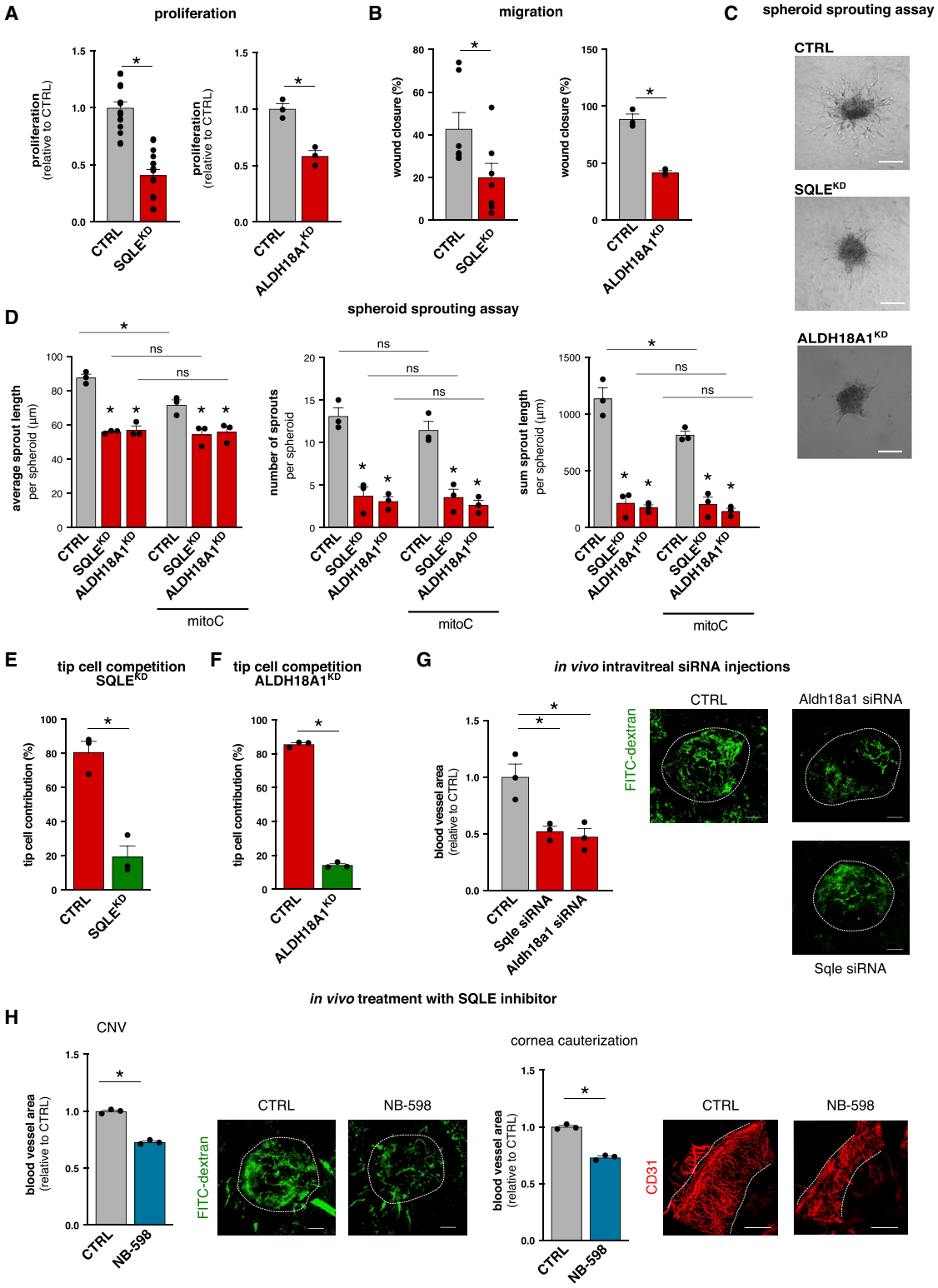

Figure 6. Metabolic Target Validation

(A) ^{3}H-thymidine incorporation in DNA assay upon SQLE (mean ± SEM, n = 16, *p < 0.05, unpaired two-tailed t test) or ALDH18A1 (mean ± SEM, n = 3, *p < 0.05, unpaired two-tailed t test) silencing (KD denotes shRNA knockdown).

(B) Scratch wound migration assay with control and SQLE (mean ± SEM, n = 7, *p < 0.05, unpaired two-tailed t test) or Aldh18a1 (mean ± SEM, n = 3, *p < 0.05, unpaired two-tailed t test) silenced ECs.

(legend continued on next page)

datasets revealed that *Aldh18a1* and *Sqle* were among the most consistently induced genes in TECs (Figures 5C and 5D; Table S5). *Aldh18a1* encodes pyrroline-5-carboxylate-synthase (P5CS), the rate-controlling enzyme of proline and collagen biosynthesis, a pathway that was consistently upregulated in angiogenic ECs in tumors and CNV (Figures S5B and S5C). *Sqle* encodes squalene monooxygenase, a rate-limiting enzyme in cholesterol biosynthesis (Cerqueira et al., 2016).

Functional Validation of Selected Targets

To functionally validate the role of *ALDH18A1* and *SQLE* in vessel sprouting, we silenced these genes (Figures S5D–S5G), which impaired EC proliferation and migration, vessel sprouting (Figures 6A–6D), and EC tip cell competitivity (Figures 6E and 6F). To explore global expression changes induced by SQLE and ALDH18A1 silencing, we performed multi-omics analysis. Transcriptomics analysis confirmed decreased expression of genes involved in cell proliferation and DNA replication in silenced cells (Figures S6A and S6B). These results were corroborated at the protein level by proteomics analysis (Figure S6C). Targeted metabolomics showed that SQLE and ALDH18A1 silencing did not affect the energy charge (Figure S6D), but confirmed that *Aldh18a1* knockdown lowered the levels of proline and hydroxyproline, a surrogate for collagen content (Stoilov et al., 2018) (Figures S6E and S6F). Finally, *in vivo* intraocular treatment with siRNAs against *Sqle* and *Aldh18a1* decreased the expression levels of these targets in CNV-ECs (Figure S6G) and inhibited neovascularization of laser-induced choroid (Figure 6G). To explore potential therapeutic relevance, we used NB-598 to pharmacologically inhibit SQLE *in vivo* and observed a reduction in both corneal angiogenesis and CNV (Figure 6H).

DISCUSSION

Objectives of this study were (1) to construct a taxonomy of CECs and CNV-ECs, (2) to characterize the heterogeneity of metabolic gene expression signatures of different ECs at the single-cell level, (3) to explore if and how angiogenic ECs reprogram their metabolic transcriptome signature during pathological angiogenesis, and (4) to design an integrated analytical approach to identify angiogenic targets regulating EC metabolism, not previously known to co-determine pathological angiogenesis.

We constructed a CEC/CNV-EC taxonomy and identified 18 choroidal EC phenotypes, of which 8 were previously not recognized, and characterized transcription factors, predicted to be involved in the differentiation of different choroidal ECs. The availability of this choroidal CEC/CNV-EC taxonomy, as well as a previously in-house constructed lung NEC/TEC taxonomy (Goveia et al., 2020), which we now used to analyze metabolic gene expression, enabled us to characterize metabolic gene expression heterogeneity in sprouting ECs across two tissues and diseases.

The metabolic transcriptome diversity was most outspoken for TECs and, remarkably, TEC phenotypes expressed distinct metabolic transcriptome signatures. Presumably, this complex metabolic transcriptome heterogeneity is required for EC phenotypes to execute their specialized functions in different vascular compartments. However, given that the micro-environment can influence cellular metabolism (Muir et al., 2018), part of the heterogeneity can possibly also be attributed to different environmental signals in distinct vascular compartments. This may partly explain why tip and immature ECs had a stronger glycolytic gene signature in tumors than in CNV, possibly evoked by the harsher nutrient-deprived environment and larger abundance of metabolism-altering signals in the tumor as compared to the CNV (Lyssiotis and Kimmelman, 2017) .

The EC taxonomies in the eye and lung offer integrated comparison of EC phenotypes across tissues and diseases. Even though tissue-type-specific EC phenotypes were recognized, angiogenic ECs in CNV and tumors seemed to form and maintain neovessels by developing similar EC phenotypes, including proliferating, tip, immature, and neophalanx ECs. Across diseases and tissues, angiogenic ECs congruently upregulated the expression of non-metabolic marker genes, as well as metabolic genes involved in OXPHOS, glycolysis, TCA cycle, nucleotide biosynthesis, and mRNA metabolism. Hence, blood vessels seem to sprout by inducing the differentiation of largely similar EC phenotypes across diseases and tissues. Tumors have been named "non-healing wounds" and angiogenesis of tumors may thus build on similar principles as a CNV wound (Dvorak, 1986). Nonetheless, tissue- and disease-specific differences in metabolic transcriptome profiles were observed, likely in part due to differences in micro-environmental conditions.

Trajectory inference analysis predicted that the hierarchy of angiogenic phenotypes is derived from pcv ECs and that phenotypic differentiation is associated with plastic metabolic gene expression reprogramming, suggesting that metabolic plasticity supports phenotypic plasticity. Early morphological studies suggested that vessel sprouting originates from this venous vascular bed (Folkman, 1982), but using *in silico* lineage tracing, we identified a differentiation trajectory of venous ECs over intermediate transitioning immature ECs to tip ECs and later to more mature neophalanx ECs.

Another objective of this study was to explore whether metabolic signatures of individual ECs could be utilized for the discovery of metabolic genes, previously not recognized to fuel vessel

(C) Bright field photographs of control, ALDH18A1^{KD}, and SQLE^{KD} EC spheroids. Scale bar, 100 μm.
(D) Morphometric quantification of the number of sprouts, average, and cumulative sprout length for control, SQLE^{KD}, and ALDH18A1^{KD} spheroids with or without MitoC treatment (mean ± SEM, n = 3 for all parameters, *p < 0.05, unpaired two-tailed t test).
(E and F) Mosaic EC spheroid competition of control (red), SQLE^{KD} (E), or ALDH18A1^{KD} (F) (green) ECs. Quantification of the fraction of tip cells with the indicated genotype. Scale bar, 50 μm. Data are mean ± SEM, n = 3, *p < 0.05 by unpaired two-tailed t test.
(G) Quantification of CNV blood vessel area in mice treated with control siRNA (CTRL) or siRNA against murine *Sqle* or *Aldh18a1*. Representative images are shown on the right. Scale bars, 75 μm. Data are mean ± SEM, n = 3 independent experiments each using six mice per group, *p < 0.05, unpaired two-tailed t test.
(H) Quantification of CNV (left) and corneal angiogenesis upon corneal cauterization-induced injury (right) in mice treated with vehicle (CTRL) or NB-598 (an SQLE blocker). Representative micrographs are shown on the right. Scale bars, 75 μm (CNV) and 500 μm (cornea). Data are mean ± SEM, n = 3 independent experiments each using six mice per group, *p < 0.05, unpaired two-tailed t test.
See also Figures S5 and S6.

sprouting. Hypothesizing that genes that were conservedly upregulated across diseases and species represent robust candidates, we performed an integrated multi-layered approach combining scRNA-seq of ECs from different tissues/diseases, congruency transcriptome analysis, genome-scale metabolic modeling, and cross-species meta-analysis to identify conserved angiogenic metabolic targets, i.e., *Sqle* for biomass synthesis and *Aldh18A* for collagen synthesis. Functional validation revealed that silencing of these targets impaired vessel sprouting *in vitro* and inhibited pathological ocular angiogenesis *in vivo*. While it was not the primary goal to develop new AAT strategies, but rather to provide proof of principle of the integrated approach, the identified metabolic targets might nonetheless deserve further attention for AAT development, though an EC-selective drug delivery approach would then be desirable.

Limitations of Study

We acknowledge limitations of our study. First, the inferred biological role and topographical localization in the vasculature of each EC phenotype and the computational trajectory inference analysis are putative/predicted and require additional marker gene identification and functional validation to probe their biological roles/principles and anatomical topography. Second, the contribution of the resident ESCs to angiogenesis and the precise mechanisms of how Aldh18a1 and Sqle regulate EC migration/proliferation and EC metabolism require further study. Third, transcript levels and metabolic modeling by GEMs do not fully capture the complexity of metabolism (metabolic fluxes, enzyme activity, and metabolite levels). However, gene signatures and GEM modeling have been proven to be predictive of the metabolic flux changes in ECs (Bruning et al., 2018; Cantelmo et al., 2016; Kalucka et al., 2018; McGarrity et al., 2018; Patella et al., 2015; Vandekeere et al., 2018). Fourth, we expect that future exploration of our dataset using newly developed pre-processing and analysis algorithms might further fine-tune our analysis and interpretation. Finally, the current data await future development of novel technology to quantify metabolism at the single-cell level in ECs, but the potential of using an integrated analysis to overcome technical limitations in metabolic target prioritization is demonstrated by the validation of the functional role of the selected candidates (Sqle and Aldh18A) in vessel sprouting *in vivo*.

To maximize resource value, we provide accompanying data exploration web tools—available at https://www.vibcancer.be/software-tools/Murine_ECTax and https://www.vibcancer.be/software-tools/scCycle, and via the publicly available added-value database EndoDB (Khan et al., 2019).

STAR★METHODS

Detailed methods are provided in the online version of this paper and include the following:

- KEY RESOURCES TABLE
- LEAD CONTACT AND MATERIALS AVAILABILITY
- EXPERIMENTAL MODEL AND SUBJECT DETAILS
  - Patient Material and Choroid EC Isolation
  - Mice
  - Mouse Model of Choroidal Neovascularization
  - Murine Choroid Endothelial Cell Isolation
  - Mouse model of Lewis Lung Carcinoma
  - Cell Lines and Primary Cell Culture
- METHOD DETAILS
  - *In Vitro* Functional Assays
  - Knockdown Strategy
  - Treatment with Inhibitor in the Murine Ocular Models
  - Murine Choroid Immunostaining
  - RNA Isolation and Quantitative RT-PCR
  - Single-cell Droplet-based RNA Sequencing
  - Single-cell Transcriptomics Analysis
  - Quality Control and Data Normalization
  - *In Silico* EC Selection
  - Batch Effect Correction
  - Feature Selection and Dimensionality Reduction
  - EC Cluster Identification
  - Marker Gene Analysis
  - Cluster Annotation
  - Gene Set Variation Analysis
  - Evaluation of Dissociation Artifacts
  - Heatmap Analysis
  - Trajectory Inference
  - Jaccard Similarity Analysis
  - Gene Set Enrichment Analysis
  - Metabolic Gene Expression Analysis and Pathway Mapping
  - Cell Cycle Pseudotime Analysis
  - Development of a Multivariate Model to Predict Cell Cycle Pseudotime
  - Pathway and Transcription Factor Activity Analysis
  - Bulk RNA-sequencing Analysis
  - Proteomics Sample Preparation
  - Proteomics LC-MS/MS and Data Analysis
  - Metabolomics and Data Analysis
  - Meta-analysis of Transcriptomics Data
  - RNAscope *In Situ* Hybridization and Quantification
  - Cytometry by Time of Flight Mass Cytometry (CyTOF)
  - CyTOF Data Analysis
  - Curation of a GEM Model
  - Development of an EC-tailored GEM
  - Development of EC Tailored Objective Functions
  - Development of an Angiogenic CEC-GEM Model
  - Prediction of Essential Genes in the Angiogenic CEC Model
- QUANTIFICATION AND STATISTICAL ANALYSIS
- DATA AND CODE AVAILABILITY
  - Data Resources
  - Software

SUPPLEMENTAL INFORMATION

Supplemental Information can be found online at https://doi.org/10.1016/j.cmet.2020.03.009.

ACKNOWLEDGMENTS

We acknowledge the help of A. Bouché, T. Van Brussel, R. Schepers, M. Pellemans, L. Roussel, and I. Van Hove for technical assistance. We also gratefully acknowledge the expert advice and help of J. Qian, B. Boeckx, and D. Lambrechts. Funding was provided by Fonds voor Wetenschappelijk Onderzoek (FWO; to K.R., J.G., J.K., and L.T.); a Marie Curie-IEF Fellowship (to K.D.F.);

Bettencourt Schueller Foundation (to L.T.); the Lundbeck Foundation (R219–2016-1375) and DFF Sapere Aude Starting Grant (8048-00072A) (to L.L.); University of Antwerp (to L.-A.T., in part); Strategisch Basisonderzoek FWO-Vlaanderen (to V.G.); the Austrian Science Fund (FWF) (J3730-B26; to A.P.); the Else Kröner-Fresenius-Stiftung and the Fritz Thyssen Stiftung (10.16.2.017MN; to L.-C.C.); Kom op Tegen Kanker (to S.K.); the Sanming Project of Medicine in Shenzhen (SZSM201612074), BGI-Research, the Danish Research Council for Independent Research (DFF–1337–00128), the Sapere Aude Young Research Talent Prize (DFF-1335–00763A), and Aarhus University Strategic Grant (AU-iCRISPR) (to L.B. and Y. Luo); the State Key Laboratory of Ophthalmology, Zhongshan Ophthalmic Center at the Sun Yat-Sen University, and the National Natural Science Foundation of China (81670855), a Guangdong Province Leading Expert Program grant, and the Key Program of Guangzhou Scientific Research Plan (3030901006074) (to X.L.); and the VIB TechWatch Program, long-term structural Methusalem funding from the Flemish Government, FWO, Foundation against Cancer (2016-078), Kom op Tegen Kanker, ERC Proof of Concept (ERC-713758), and ERC Advanced Research Grant (EU-ERC743074) (to P.C.).

AUTHOR CONTRIBUTIONS

K.R. and J.G. designed and analyzed all experiments. M.G.-C. performed *in vivo* experiments. A.S. developed GEMs. J.G., J.K., M.G.-C., L.T., A.P., and L.-C.C. set up endothelial cell isolation protocols. L.T. and K.D.F. performed *in vitro* experiments. F.T. performed bioinformatics analysis and implemented the online databases. N.E. provided human choroid samples. J.K., L.P.M.H.d.R., Y.Z., L. Sokol, V.G., D.P., F.D.S., F.J.T.S., R.J.M., and Y. Liu performed CyTOF measurements. K.R., J.K., M.G.-C., L.T., L. Sokol, L.-A.T., V.G., and L.-C.C. prepared scRNA-seq samples. L.L., B.T., and Y. Luo performed 10x single-cell sequencing. S.K. processed scRNA-seq data. S.S. and G.C. performed hydroxyproline measurements. F.D.S., S.V., T.V.B., G.E., P.D.H., M.D., L. Schoonjans, J.W., L.B., H.Y., B.T., X.L., and Y. Luo provided advice and discussed results. K.R., J.G., and P.C. wrote the manuscript. P.C. conceptualized the study. All authors discussed results and commented on the manuscript.

DECLARATION OF INTERESTS

The authors declare no competing interests.

Received: July 11, 2019
Revised: December 20, 2019
Accepted: March 9, 2020
Published: April 7, 2020

REFERENCES

Aibar, S., González-Blas, C.B., Moerman, T., Huynh-Thu, V.A., Imrichova, H., Hulselmans, G., Rambow, F., Marine, J.C., Geurts, P., Aerts, J., et al. (2017). SCENIC: single-cell regulatory network inference and clustering. Nat. Methods *14*, 1083–1086.

Ambati, J., and Fowler, B.J. (2012). Mechanisms of age-related macular degeneration. Neuron *75*, 26–39.

Apostolidis, S.A., Stifano, G., Tabib, T., Rice, L.M., Morse, C.M., Kahaleh, B., and Lafyatis, R. (2018). Single cell RNA sequencing identifies HSPG2 and APLNR as markers of endothelial cell injury in systemic sclerosis skin. Front. Immunol. *9*, 2191.

Atkins, G.B., and Jain, M.K. (2007). Role of Krüppel-like transcription factors in endothelial biology. Circ. Res. *100*, 1686–1695.

Aurich, M.K., Fleming, R.M.T., and Thiele, I. (2016). MetaboTools: a comprehensive toolbox for analysis of genome-scale metabolic models. Front. Physiol. *7*, 327.

Barankiewicz, J., Kaplinsky, C., and Cohen, A. (1986). Modification of ribonucleotide and deoxyribonucleotide metabolism in interferon-treated human B-lymphoblastoid cells. J. Interferon Res. *6*, 717–727.

Baydoun, A.R., Emery, P.W., Pearson, J.D., and Mann, G.E. (1990). Substrate-dependent regulation of intracellular amino acid concentrations in cultured bovine aortic endothelial cells. Biochem. Biophys. Res. Commun. *173*, 940–948.

Becker, S.A., and Palsson, B.O. (2008). Context-specific metabolic networks are consistent with experiments. PLoS Comput. Biol. *4*, e1000082.

Bjorklund, G., Svanberg, E., Dadar, M., Card, D.J., Chirumbolo, S., Harrington, D.J., and Aaseth, J. (2018). The role of matrix Gla protein (MGP) in vascular calcification. Curr. Med. Chem. Published July 15, 2018. https://doi.org/10.2174/0929867325666180716104159.

Blaauwgeers, H.G., Holtkamp, G.M., Rutten, H., Witmer, A.N., Koolwijk, P., Partanen, T.A., Alitalo, K., Kroon, M.E., Kijlstra, A., van Hinsbergh, V.W., and Schlingemann, R.O. (1999). Polarized vascular endothelial growth factor secretion by human retinal pigment epithelium and localization of vascular endothelial growth factor receptors on the inner choriocapillaris. Evidence for a trophic paracrine relation. Am. J. Pathol. *155*, 421–428.

Bradshaw, A.D., and Sage, E.H. (2001). SPARC, a matricellular protein that functions in cellular differentiation and tissue response to injury. J. Clin. Invest. *107*, 1049–1054.

Bruning, U., Morales-Rodriguez, F., Kalucka, J., Goveia, J., Taverna, F., Queiroz, K.C.S., Dubois, C., Cantelmo, A.R., Chen, R., Loroch, S., et al. (2018). Impairment of angiogenesis by fatty acid synthase inhibition involves mTOR malonylation. Cell Metab. *28*, 866–880.e15.

Cannoodt, R., Saelens, W., Sichien, D., Tavernier, S., Janssens, S., Guilliams, M., Lambrecht, B., Preter, K.D., and Saeys, Y. (2016). SCORPIUS improves trajectory inference and identifies novel modules in dendritic cell development. bioRxiv. https://doi.org/10.1101/079509.

Cantelmo, A.R., Conradi, L.C., Brajic, A., Goveia, J., Kalucka, J., Pircher, A., Chaturvedi, P., Hol, J., Thienpont, B., Teuwen, L.A., et al. (2016). Inhibition of the glycolytic activator PFKFB3 in endothelium induces tumor vessel normalization, impairs metastasis, and improves chemotherapy. Cancer Cell *30*, 968–985.

Carmeliet, P., and Jain, R.K. (2011). Molecular mechanisms and clinical applications of angiogenesis. Nature *473*, 298–307.

Cerqueira, N.M.F.S.A., Oliveira, E.F., Gesto, D.S., Santos-Martins, D., Moreira, C., Moorthy, H.N., Ramos, M.J., and Fernandes, P.A. (2016). Cholesterol biosynthesis: a mechanistic overview. Biochemistry *55*, 5483–5506.

Chambers, M.C., Maclean, B., Burke, R., Amodei, D., Ruderman, D.L., Neumann, S., Gatto, L., Fischer, B., Pratt, B., Egertson, J., et al. (2012). A cross-platform toolkit for mass spectrometry and proteomics. Nat. Biotechnol. *30*, 918–920.

Chen, L. (2009). Ocular lymphatics: state-of-the-art review. Lymphology *42*, 66–76.

Corada, M., Orsenigo, F., Morini, M.F., Pitulescu, M.E., Bhat, G., Nyqvist, D., Breviario, F., Conti, V., Briot, A., Iruela-Arispe, M.L., et al. (2013). Sox17 is indispensable for acquisition and maintenance of arterial identity. Nat. Commun. *4*, 2609.

Corey, D.M., Rinkevich, Y., and Weissman, I.L. (2016). Dynamic patterns of clonal evolution in tumor vasculature underlie alterations in lymphocyte-endothelial recognition to foster tumor immune escape. Cancer Res. *76*, 1348–1353.

Cox, J., and Mann, M. (2008). MaxQuant enables high peptide identification rates, individualized p.p.b.-range mass accuracies and proteome-wide protein quantification. Nat. Biotechnol. *26*, 1367–1372.

Creemers, L.B., Jansen, D.C., van Veen-Reurings, A., van den Bos, T., and Everts, V. (1997). Microassay for the assessment of low levels of hydroxyproline. Biotechniques *22*, 656–658.

De Bock, K., Georgiadou, M., Schoors, S., Kuchnio, A., Wong, B.W., Cantelmo, A.R., Quaegebeur, A., Ghesquière, B., Cauwenberghs, S., Eelen, G., et al. (2013). Role of PFKFB3-driven glycolysis in vessel sprouting. Cell *154*, 651–663.

de Lichtenberg, U., Jensen, L.J., Fausbøll, A., Jensen, T.S., Bork, P., and Brunak, S. (2005). Comparison of computational methods for the identification of cell cycle-regulated genes. Bioinformatics *21*, 1164–1171.

del Toro, R., Prahst, C., Mathivet, T., Siegfried, G., Kaminker, J.S., Larrivee, B., Breant, C., Duarte, A., Takakura, N., Fukamizu, A., et al. (2010). Identification

and functional analysis of endothelial tip cell-enriched genes. Blood *116*, 4025–4033.

dela Paz, N.G., and D'Amore, P.A. (2009). Arterial versus venous endothelial cells. Cell Tissue Res. *335*, 5–16.

Desouki, A.A., Jarre, F., Gelius-Dietrich, G., and Lercher, M.J. (2015). CycleFreeFlux: efficient removal of thermodynamically infeasible loops from flux distributions. Bioinformatics *31*, 2159–2165.

Diebold, L.P., Gil, H.J., Gao, P., Martinez, C.A., Weinberg, S.E., and Chandel, N.S. (2019). Mitochondrial complex III is necessary for endothelial cell proliferation during angiogenesis. Nat Metab *1*, 158–171.

Duarte, N.C., Becker, S.A., Jamshidi, N., Thiele, I., Mo, M.L., Vo, T.D., Srivas, R., and Palsson, B.Ø. (2007). Global reconstruction of the human metabolic network based on genomic and bibliomic data. Proc. Natl. Acad. Sci. USA *104*, 1777–1782.

Dvorak, H.F. (1986). Tumors: wounds that do not heal. Similarities between tumor stroma generation and wound healing. N. Engl. J. Med. *315*, 1650–1659.

Eales, K.L., Hollinshead, K.E., and Tennant, D.A. (2016). Hypoxia and metabolic adaptation of cancer cells. Oncogenesis *5*, e190.

Eastoe, J.E. (1955). The amino acid composition of mammalian collagen and gelatin. Biochem. J. *61*, 589–600.

Eelen, G., de Zeeuw, P., Treps, L., Harjes, U., Wong, B.W., and Carmeliet, P. (2018). Endothelial cell metabolism. Physiol. Rev. *98*, 3–58.

Epstein, M. (2016). Matrix Gla-protein (MGP) not only inhibits calcification in large arteries but also may be renoprotective: connecting the dots. EBioMedicine *4*, 16–17.

Félétou, M., Huang, Y., and Vanhoutte, P.M. (2011). Endothelium-mediated control of vascular tone: COX-1 and COX-2 products. Br. J. Pharmacol. *164*, 894–912.

Fitzgerald, G., Soro-Arnaiz, I., and De Bock, K. (2018). The Warburg effect in endothelial cells and its potential as an anti-angiogenic target in cancer. Front. Cell Dev. Biol. *6*, 100.

Folkman, J. (1982). Angiogenesis: initiation and control. Ann. N Y Acad. Sci. *401*, 212–227.

García-Caballero, M., Zecchin, A., Souffreau, J., Truong, A.-C.K., Teuwen, L.-A., Vermaelen, W., Martín-Pérez, R., de Zeeuw, P., Bouché, A., Vinckier, S., et al. (2019). Role and therapeutic potential of dietary ketone bodies in lymph vessel growth. Nature Metabolism *1*, 666–675.

Goveia, J., Rohlenova, K., Taverna, F., Treps, L., Conradi, L.C., Pircher, A., Geldhof, V., de Rooij, L.P.M.H., Kalucka, J., Sokol, L., et al. (2020). An integrated gene expression landscape profiling approach to identify lung tumor endothelial cell heterogeneity and angiogenic candidates. Cancer Cell *37*, 21–36.e13.

Haghverdi, L., Lun, A.T.L., Morgan, M.D., and Marioni, J.C. (2018). Batch effects in single-cell RNA-sequencing data are corrected by matching mutual nearest neighbors. Nat. Biotechnol. *36*, 421–427.

Hänzelmann, S., Castelo, R., and Guinney, J. (2013). GSVA: gene set variation analysis for microarray and RNA-seq data. BMC Bioinformatics *14*, 7.

Haraldsdóttir, H.S., Cousins, B., Thiele, I., Fleming, R.M.T., and Vempala, S. (2017). CHRR: coordinate hit-and-run with rounding for uniform sampling of constraint-based models. Bioinformatics *33*, 1741–1743.

Hart, T., Komori, H.K., LaMere, S., Podshivalova, K., and Salomon, D.R. (2013). Finding the active genes in deep RNA-seq gene expression studies. BMC Genomics *14*, 778.

Hazell, G.G., Peachey, A.M., Teasdale, J.E., Sala-Newby, G.B., Angelini, G.D., Newby, A.C., and White, S.J. (2016). PI16 is a shear stress and inflammation-regulated inhibitor of MMP2. Sci. Rep. *6*, 39553.

Heindl, L.M., Kaser-Eichberger, A., Schlereth, S.L., Bock, F., Regenfuss, B., Reitsamer, H.A., McMenamin, P., Lutty, G.A., Maruyama, K., Chen, L., et al. (2015). Sufficient evidence for lymphatics in the developing and adult human choroid? Invest. Ophthalmol. Vis. Sci. *56*, 6709–6710.

Heirendt, L., Arreckx, S., Pfau, T., Mendoza, S.N., Richelle, A., Heinken, A., Haraldsdóttir, H.S., Wachowiak, J., Keating, S.M., Vlasov, V., et al. (2019). Creation and analysis of biochemical constraint-based models using the COBRA Toolbox v.3.0. Nat. Protoc. *14*, 639–702.

Hong, F., Breitling, R., McEntee, C.W., Wittner, B.S., Nemhauser, J.L., and Chory, J. (2006). RankProd: a bioconductor package for detecting differentially expressed genes in meta-analysis. Bioinformatics *22*, 2825–2827.

Huang, H., Vandekeere, S., Kalucka, J., Bierhansl, L., Zecchin, A., Brüning, U., Visnagri, A., Yuldasheva, N., Goveia, J., Cruys, B., et al. (2017). Role of glutamine and interlinked asparagine metabolism in vessel formation. EMBO J. *36*, 2334–2352.

Hwangbo, C., Wu, J., Papangeli, I., Adachi, T., Sharma, B., Park, S., Zhao, L., Ju, H., Go, G.W., Cui, G., et al. (2017). Endothelial APLNR regulates tissue fatty acid uptake and is essential for apelin's glucose-lowering effects. Sci. Transl. Med. *9*, https://doi.org/10.1126/scitranslmed.aad4000.

Iñiguez, M.A., Rodríguez, A., Volpert, O.V., Fresno, M., and Redondo, J.M. (2003). Cyclooxygenase-2: a therapeutic target in angiogenesis. Trends Mol. Med. *9*, 73–78.

Jain, R.K. (2014). Antiangiogenesis strategies revisited: from starving tumors to alleviating hypoxia. Cancer Cell *26*, 605–622.

Jeong, H.W., Hernández-Rodríguez, B., Kim, J., Kim, K.P., Enriquez-Gasca, R., Yoon, J., Adams, S., Schöler, H.R., Vaquerizas, J.M., and Adams, R.H. (2017). Transcriptional regulation of endothelial cell behavior during sprouting angiogenesis. Nat. Commun. *8*, 726.

Kalucka, J., Bierhansl, L., Conchinha, N.V., Missiaen, R., Elia, I., Brüning, U., Scheinok, S., Treps, L., Cantelmo, A.R., Dubois, C., et al. (2018). Quiescent endothelial cells upregulate fatty acid β-oxidation for vasculoprotection via redox homeostasis. Cell Metab. *28*, 881–894.e13.

Kanda, T., Brown, J.D., Orasanu, G., Vogel, S., Gonzalez, F.J., Sartoretto, J., Michel, T., and Plutzky, J. (2009). PPARgamma in the endothelium regulates metabolic responses to high-fat diet in mice. J. Clin. Invest. *119*, 110–124.

Khan, S., Taverna, F., Rohlenova, K., Treps, L., Geldhof, V., de Rooij, L., Sokol, L., Pircher, A., Conradi, L.C., Kalucka, J., et al. (2019). EndoDB: a database of endothelial cell transcriptomics data. Nucleic Acids Res. *47*, D736–D744.

Kim, M.K., and Lun, D.S. (2014). Methods for integration of transcriptomic data in genome-scale metabolic models. Comput. Struct. Biotechnol. J. *11*, 59–65.

Koina, M.E., Baxter, L., Adamson, S.J., Arfuso, F., Hu, P., Madigan, M.C., and Chan-Ling, T. (2015). Evidence for lymphatics in the developing and adult human choroid. Invest. Ophthalmol. Vis. Sci. *56*, 1310–1327.

Lambert, V., Lecomte, J., Hansen, S., Blacher, S., Gonzalez, M.L., Struman, I., Sounni, N.E., Rozet, E., de Tullio, P., Foidart, J.M., et al. (2013). Laser-induced choroidal neovascularization model to study age-related macular degeneration in mice. Nat. Protoc. *8*, 2197–2211.

Langmead, B., and Salzberg, S.L. (2012). Fast gapped-read alignment with Bowtie 2. Nat. Methods *9*, 357–359.

Levandowsky, M., and Winter, D. (1971). Distance between Sets. Nature *234*, 34.

Li, X., Kumar, A., and Carmeliet, P. (2019). Metabolic pathways fueling the endothelial cell drive. Annu. Rev. Physiol. *81*, 483–503.

Luo, W., and Brouwer, C. (2013). Pathview: an R/Bioconductor package for pathway-based data integration and visualization. Bioinformatics *29*, 1830–1831.

Lyssiotis, C.A., and Kimmelman, A.C. (2017). Metabolic interactions in the tumor microenvironment. Trends Cell Biol. *27*, 863–875.

Mahadevan, R., and Schilling, C.H. (2003). The effects of alternate optimal solutions in constraint-based genome-scale metabolic models. Metab. Eng. *5*, 264–276.

Manavski, Y., Lucas, T., Glaser, S.F., Dorsheimer, L., Günther, S., Braun, T., Rieger, M.A., Zeiher, A.M., Boon, R.A., and Dimmeler, S. (2018). Clonal expansion of endothelial cells contributes to ischemia-induced neovascularization. Circ. Res. *122*, 670–677.

Marneros, A.G., She, H., Zambarakji, H., Hashizume, H., Connolly, E.J., Kim, I., Gragoudas, E.S., Miller, J.W., and Olsen, B.R. (2007). Endogenous endostatin inhibits choroidal neovascularization. FASEB J. *21*, 3809–3818.

McCandless, E.E., Piccio, L., Woerner, B.M., Schmidt, R.E., Rubin, J.B., Cross, A.H., and Klein, R.S. (2008). Pathological expression of CXCL12 at the blood-brain barrier correlates with severity of multiple sclerosis. Am. J. Pathol. *172*, 799–808.

McCormick, S.M., Eskin, S.G., McIntire, L.V., Teng, C.L., Lu, C.M., Russell, C.G., and Chittur, K.K. (2001). DNA microarray reveals changes in gene expression of shear stressed human umbilical vein endothelial cells. Proc. Natl. Acad. Sci. USA *98*, 8955–8960.

McDonald, A.I., Shirali, A.S., Aragón, R., Ma, F., Hernandez, G., Vaughn, D.A., Mack, J.J., Lim, T.Y., Sunshine, H., Zhao, P., et al. (2018). Endothelial regeneration of large vessels is a biphasic process driven by local cells with distinct proliferative capacities. Cell Stem Cell *23*, 210–225.e6.

McGarrity, S., Anuforo, Ó., Halldórsson, H., Bergmann, A., Halldórsson, S., Palsson, S., Henriksen, H.H., Johansson, P.I., and Rolfsson, Ó. (2018). Metabolic systems analysis of LPS induced endothelial dysfunction applied to sepsis patient stratification. Sci. Rep. *8*, 6811.

McLeod, D.S., Lefer, D.J., Merges, C., and Lutty, G.A. (1995). Enhanced expression of intracellular adhesion molecule-1 and P-selectin in the diabetic human retina and choroid. Am. J. Pathol. *147*, 642–653.

Mondor, I., Jorquera, A., Sene, C., Adriouch, S., Adams, R.H., Zhou, B., Wienert, S., Klauschen, F., and Bajénoff, M. (2016). Clonal proliferation and stochastic pruning orchestrate lymph node vasculature remodeling. Immunity *45*, 877–888.

Muir, A., Danai, L.V., and Vander Heiden, M.G. (2018). Microenvironmental regulation of cancer cell metabolism: implications for experimental design and translational studies. Dis. Model. Mech. *11*, https://doi.org/10.1242/dmm.035758.

Murphy, E.J., Joseph, L., Stephens, R., and Horrocks, L.A. (1992). Phospholipid composition of cultured human endothelial cells. Lipids *27*, 150–153.

Naito, H., Kidoya, H., Sakimoto, S., Wakabayashi, T., and Takakura, N. (2012). Identification and characterization of a resident vascular stem/progenitor cell population in preexisting blood vessels. EMBO J. *31*, 842–855.

Naschberger, E., Liebl, A., Schellerer, V.S., Schütz, M., Britzen-Laurent, N., Kölbel, P., Schaal, U., Haep, L., Regensburger, D., Wittmann, T., et al. (2016). Matricellular protein SPARCL1 regulates tumor microenvironment-dependent endothelial cell heterogeneity in colorectal carcinoma. J. Clin. Invest. *126*, 4187–4204.

Neve, A., Cantatore, F.P., Maruotti, N., Corrado, A., and Ribatti, D. (2014). Extracellular matrix modulates angiogenesis in physiological and pathological conditions. BioMed Res. Int. *2014*, 756078.

O'Brien, E.J., Monk, J.M., and Palsson, B.O. (2015). Using genome-scale models to predict biological capabilities. Cell *161*, 971–987.

Pagliarini, R., Castello, R., Napolitano, F., Borzone, R., Annunziata, P., Mandrile, G., De Marchi, M., Brunetti-Pierri, N., and di Bernardo, D. (2016). In silico modeling of liver metabolism in a human disease reveals a key enzyme for histidine and histamine homeostasis. Cell Rep. *15*, 2292–2300.

Patel, J., Seppanen, E.J., Rodero, M.P., Wong, H.Y., Donovan, P., Neufeld, Z., Fisk, N.M., Francois, M., and Khosrotehrani, K. (2017). Functional definition of progenitors versus mature endothelial cells reveals key SoxF-dependent differentiation process. Circulation *135*, 786–805.

Patella, F., Schug, Z.T., Persi, E., Neilson, L.J., Erami, Z., Avanzato, D., Maione, F., Hernandez-Fernaud, J.R., Mackay, G., Zheng, L., et al. (2015). Proteomics-based metabolic modeling reveals that fatty acid oxidation (FAO) controls endothelial cell (EC) permeability. Mol. Cell. Proteomics *14*, 621–634.

Perez-Riverol, Y., Csordas, A., Bai, J., Bernal-Llinares, M., Hewapathirana, S., Kundu, D.J., Inuganti, A., Griss, J., Mayer, G., Eisenacher, M., et al. (2019). The PRIDE database and related tools and resources in 2019: improving support for quantification data. Nucleic Acids Res. *47* (D1), D442–D450.

Phang, J.M. (2019). Proline metabolism in cell regulation and cancer biology: recent advances and hypotheses. Antioxid. Redox Signal. *30*, 635–649.

Potente, M., Gerhardt, H., and Carmeliet, P. (2011). Basic and therapeutic aspects of angiogenesis. Cell *146*, 873–887.

Pusztaszeri, M.P., Seelentag, W., and Bosman, F.T. (2006). Immunohistochemical expression of endothelial markers CD31, CD34, von Willebrand factor, and Fli-1 in normal human tissues. J. Histochem. Cytochem. *54*, 385–395.

Rastogi, B.K., and Nordøy, A. (1980). Lipid composition of cultured human endothelial cells. Thromb. Res. *18*, 629–641.

Red-Horse, K., Ueno, H., Weissman, I.L., and Krasnow, M.A. (2010). Coronary arteries form by developmental reprogramming of venous cells. Nature *464*, 549–553.

Ritchie, M.E., Phipson, B., Wu, D., Hu, Y., Law, C.W., Shi, W., and Smyth, G.K. (2015). limma powers differential expression analyses for RNA-sequencing and microarray studies. Nucleic Acids Res. *43*, e47.

Roca, C., and Adams, R.H. (2007). Regulation of vascular morphogenesis by Notch signaling. Genes Dev. *21*, 2511–2524.

Ryu, J.Y., Kim, H.U., and Lee, S.Y. (2015). Reconstruction of genome-scale human metabolic models using omics data. Integr. Biol. *7*, 859–868.

Santos, C.R., and Schulze, A. (2012). Lipid metabolism in cancer. FEBS J. *279*, 2610–2623.

Santos, A., Wernersson, R., and Jensen, L.J. (2015). Cyclebase 3.0: a multi-organism database on cell-cycle regulation and phenotypes. Nucleic Acids Res. *43*, D1140–D1144.

Sardana, M., Vasim, I., Varakantam, S., Kewan, U., Tariq, A., Koppula, M.R., Syed, A.A., Beraun, M., Drummen, N.E., Vermeer, C., et al. (2017). Inactive matrix Gla-protein and arterial stiffness in type 2 diabetes mellitus. Am. J. Hypertens. *30*, 196–201.

Satija, R., Farrell, J.A., Gennert, D., Schier, A.F., and Regev, A. (2015). Spatial reconstruction of single-cell gene expression data. Nat. Biotechnol. *33*, 495–502.

Sawada, N., and Arany, Z. (2017). Metabolic regulation of angiogenesis in diabetes and aging. Physiology (Bethesda) *32*, 290–307.

Schoors, S., De Bock, K., Cantelmo, A.R., Georgiadou, M., Ghesquière, B., Cauwenberghs, S., Kuchnio, A., Wong, B.W., Quaegebeur, A., Goveia, J., et al. (2014). Partial and transient reduction of glycolysis by PFKFB3 blockade reduces pathological angiogenesis. Cell Metab. *19*, 37–48.

Schoors, S., Bruning, U., Missiaen, R., Queiroz, K.C., Borgers, G., Elia, I., Zecchin, A., Cantelmo, A.R., Christen, S., Goveia, J., et al. (2015). Fatty acid carbon is essential for dNTP synthesis in endothelial cells. Nature *520*, 192–197.

Scialdone, A., Natarajan, K.N., Saraiva, L.R., Proserpio, V., Teichmann, S.A., Stegle, O., Marioni, J.C., and Buettner, F. (2015). Computational assignment of cell-cycle stage from single-cell transcriptome data. Methods *85*, 54–61.

Semenza, G.L. (2011). Hypoxia-inducible factor 1: regulator of mitochondrial metabolism and mediator of ischemic preconditioning. Biochim. Biophys. Acta *1813*, 1263–1268.

Shlomi, T., Benyamini, T., Gottlieb, E., Sharan, R., and Ruppin, E. (2011). Genome-scale metabolic modeling elucidates the role of proliferative adaptation in causing the Warburg effect. PLoS Comput. Biol. *7*, e1002018.

Stoilov, I., Starcher, B.C., Mecham, R.P., and Broekelmann, T.J. (2018). Measurement of elastin, collagen, and total protein levels in tissues. Methods Cell Biol. *143*, 133–146.

Strasser, G.A., Kaminker, J.S., and Tessier-Lavigne, M. (2010). Microarray analysis of retinal endothelial tip cells identifies CXCR4 as a mediator of tip cell morphology and branching. Blood *115*, 5102–5110.

Swainston, N., Smallbone, K., Hefzi, H., Dobson, P.D., Brewer, J., Hanscho, M., Zielinski, D.C., Ang, K.S., Gardiner, N.J., Gutierrez, J.M., et al. (2016). Recon 2.2: from reconstruction to model of human metabolism. Metabolomics *12*, 109.

Takabatake, Y., Sugiyama, T., Kohara, H., Matsusaka, T., Kurihara, H., Koni, P.A., Nagasawa, Y., Hamano, T., Matsui, I., Kawada, N., et al. (2009). The CXCL12 (SDF-1)/CXCR4 axis is essential for the development of renal vasculature. J. Am. Soc. Nephrol. *20*, 1714–1723.

Thiele, I., and Palsson, B.O. (2010). A protocol for generating a high-quality genome-scale metabolic reconstruction. Nat. Protoc. *5*, 93–121.

Thiriot, A., Perdomo, C., Cheng, G., Novitzky-Basso, I., McArdle, S., Kishimoto, J.K., Barreiro, O., Mazo, I., Triboulet, R., Ley, K., et al. (2017). Differential DARC/ACKR1 expression distinguishes venular from non-venular endothelial cells in murine tissues. BMC Biol. *15*, 45.

van den Brink, S.C., Sage, F., Vértesy, Á., Spanjaard, B., Peterson-Maduro, J., Baron, C.S., Robin, C., and van Oudenaarden, A. (2017). Single-cell sequencing reveals dissociation-induced gene expression in tissue subpopulations. Nat. Methods *14*, 935–936.

Vandekeere, S., Dubois, C., Kalucka, J., Sullivan, M.R., García-Caballero, M., Goveia, J., Chen, R., Diehl, F.F., Bar-Lev, L., Souffreau, J., et al. (2018). Serine synthesis via PHGDH is essential for heme production in endothelial cells. Cell Metab. *28*, 573–587.e13.

Vanlandewijck, M., He, L., Mäe, M.A., Andrae, J., Ando, K., Del Gaudio, F., Nahar, K., Lebouvier, T., Laviña, B., Gouveia, L., et al. (2018). A molecular atlas of cell types and zonation in the brain vasculature. Nature *554*, 475–480.

Vartanian, R.K., and Weidner, N. (1994). Correlation of intratumoral endothelial cell proliferation with microvessel density (tumor angiogenesis) and tumor cell proliferation in breast carcinoma. Am. J. Pathol. *144*, 1188–1194.

Wagenseil, J.E., and Mecham, R.P. (2012). Elastin in large artery stiffness and hypertension. J. Cardiovasc. Transl. Res. *5*, 264–273.

Wakabayashi, T., Naito, H., Takara, K., Kidoya, H., Sakimoto, S., Oshima, Y., Nishida, K., and Takakura, N. (2013). Identification of vascular endothelial side population cells in the choroidal vessels and their potential role in age-related macular degeneration. Invest. Ophthalmol. Vis. Sci. *54*, 6686–6693.

Wakabayashi, T., Naito, H., Suehiro, J.I., Lin, Y., Kawaji, H., Iba, T., Kouno, T., Ishikawa-Kato, S., Furuno, M., Takara, K., et al. (2018). CD157 marks tissue-resident endothelial stem cells with homeostatic and regenerative properties. Cell Stem Cell *22*, 384–397.e6.

Welti, J., Loges, S., Dimmeler, S., and Carmeliet, P. (2013). Recent molecular discoveries in angiogenesis and antiangiogenic therapies in cancer. J. Clin. Invest. *123*, 3190–3200.

Whitfield, M.L., Sherlock, G., Saldanha, A.J., Murray, J.I., Ball, C.A., Alexander, K.E., Matese, J.C., Perou, C.M., Hurt, M.M., Brown, P.O., and Botstein, D. (2002). Identification of genes periodically expressed in the human cell cycle and their expression in tumors. Mol. Biol. Cell *13*, 1977–2000.

Yang, S., Zhao, J., and Sun, X. (2016). Resistance to anti-VEGF therapy in neovascular age-related macular degeneration: a comprehensive review. Drug Des. Devel. Ther. *10*, 1857–1867.

Ying, Y., Ueta, T., Jiang, S., Lin, H., Wang, Y., Vavvas, D., Wen, R., Chen, Y.G., and Luo, Z. (2017). Metformin inhibits ALK1-mediated angiogenesis via activation of AMPK. Oncotarget *8*, 32794–32806.

You, L.R., Lin, F.J., Lee, C.T., DeMayo, F.J., Tsai, M.J., and Tsai, S.Y. (2005). Suppression of Notch signalling by the COUP-TFII transcription factor regulates vein identity. Nature *435*, 98–104.

Yu, G., Wang, L.G., Han, Y., and He, Q.Y. (2012). clusterProfiler: an R package for comparing biological themes among gene clusters. OMICS *16*, 284–287.

Yu, P., Alves, T.C., Kibbey, R.G., and Simons, M. (2018). Metabolic analysis of lymphatic endothelial cells. Methods Mol. Biol. *1846*, 325–334.

Zanetta, L., Marcus, S.G., Vasile, J., Dobryansky, M., Cohen, H., Eng, K., Shamamian, P., and Mignatti, P. (2000). Expression of Von Willebrand factor, an endothelial cell marker, is up-regulated by angiogenesis factors: a potential method for objective assessment of tumor angiogenesis. Int. J. Cancer *85*, 281–288.

Zhao, Q., Eichten, A., Parveen, A., Adler, C., Huang, Y., Wang, W., Ding, Y., Adler, A., Nevins, T., Ni, M., et al. (2018). Single-cell transcriptome analyses reveal endothelial cell heterogeneity in tumors and changes following antiangiogenic treatment. Cancer Res. *78*, 2370–2382.

Q6 Q7 STAR★METHODS

KEY RESOURCES TABLE

REAGENT or RESOURCE	SOURCE	IDENTIFIER
Antibodies		
Rabbit anti-human/mouse ELN	Abcam	Cat# ab21610; RRID: AB_446423
Mouse anti-human/mouse aSMA	Agilent, Dako	Cat# M0851; RRID: AB_222350
Rat anti-mouse SELP	BD Biosciences	Cat# BD553742; RRID: AB_2254315
Mouse anti-human/mouse SDF1 (CXCL12)	R&D	Cat# MAB350; RRID: AB_2088149
Mouse anti-human/mouse VEGFR2	Santa Cruz	Cat# sc-6251; RRID: AB_628431
Rabbit anti-human/mouse VWF	Agilent, Dako	Cat# A0082; RRID: AB_2315602
Rabbit anti-human/mouse LXN	Abcam	Cat# ab154744
Rabbit anti-human/mouse PlGF	Abcam	Cat# ab9542; RRID: AB_307330
Rabbit anti-human/mouse APLNR	Proteintech	Cat# 20341-1-AP
Rabbit anti-human/mouse CXCR4	Novus Biologicals	Cat# NLS1380; RRID: AB_2292628
Rabbit anti-human/mouse SPARCL1	Abcam	Cat# Ab107533; RRID: AB_10863538
Rat anti-mouse CD31	BD Biosciences	Cat# 557355; RRID: AB_396660
Goat anti-mouse CD105	R&D	Cat# AF1320; RRID: AB_354735
Rat anti-mouse CD45-PeCy7	eBioscience	Cat# 25-0451-82; RRID: AB_2734986
Rat anti-mouse CD31-FITC	eBioscience	Cat# 11-0311-85; RRID: AB_465013
Rat anti-mouse CD102-APC	Thermo Fisher Scientific	Cat# A15452; RRID: AB_2534465
Goat anti-mouse SPARC 173Yb	R&D	Cat# AF942; RRID: AB_2286625
Goat anti-mouse/human COL18A1 153Eu	R&D	Cat# AF570; RRID: AB_2081736
Rabbit anti-human SQLE	Abcam	Cat# ab189773
Rabbit anti-human ALDH18A1	Sigma-Aldrich	Cat# HPA008333; RRID: AB_1078125
Donkey anti-rat Alexa 568	Thermo Fisher Scientific	Cat# A-11077; RRID: AB_2534121
Donkey anti-mouse 488	Thermo Fisher Scientific	Cat# A-21202, RRID: AB_141607
Donkey anti-rat Alexa 488	Thermo Fisher Scientific	Cat# A-21208; RRID: AB_2535794
Donkey anti-rabbit Alexa 647	Thermo Fisher Scientific	Cat# A-31573; RRID: AB_2536183
Donkey anti-rabbit Alexa 568	Thermo Fisher Scientific	Cat# A10042; RRID: AB_2534017
Donkey anti-rabbit Alexa 488	Thermo Fisher Scientific	Cat# A-21206; RRID: 2535792
Biological Samples		
Murine choroidal and cornea neovascularization samples (study approved by the Animal Ethics Committee of the KU Leuven under protocol number P012/2014, P156/2015 and P035/2019)	This paper	N/A
Human choroidal samples (obtained from UZ Leuven Biobank, leftover material from a post-mortem multiorgan donor)	This paper	N/A
LLC orthotopic tumor samples (study approved by the Animal Ethics Committee of the KU Leuven under protocol number P012/2014 and P156/2015)	(Goveia et al., 2020)	N/A
Chemicals, Peptides, and Recombinant Proteins		
[^{3}H]-thymidine	Perkin Elmer	NET355L005MC
DMSO	Sigma-Aldrich	D2438
EDTA	VWR Chemicals	20302.293
FITC-dextran	Sigma-Aldrich	FD2000S
Glutamine	Thermo Fisher Scientific	25030149
Glycerol	Merck Millipore	1.04091.1000
Hoechst 33258	Sigma-Aldrich	B2261

(*Continued on next page*)

Continued

REAGENT or RESOURCE	SOURCE	IDENTIFIER
Isolectin B4	Thermo Fisher Scientific	*I21411*
Matrigel, growth factor reduced	Corning	356230
Mitomycin C	Sigma-Aldrich	M0503-2MG
Methylcellulose 4000 cP	Sigma-Aldrich	M0512
NB-598	MedChemExpress	HY-16343
Paraformaldehyde	Merck Millipore	8.18715.1000
ProLong Gold antifade reagent	Thermo Fisher Scientific	P36934
Sodium dodecyl sulphate	Acros Organics	230425000
Sodium pyruvate	Thermo Fisher Scientific	11360070
TCA (trichloroacetic acid)	Sigma-Aldrich	T6399
Critical Commercial Assays		
CD31 MicroBeads, mouse	Miltenyi Biotec	130-097-418
CD31 MicroBead Kit, human	Miltenyi Biotec	130-091-935
CD45 MicroBeads, mouse	Miltenyi Biotec	130-052-301
CD45 MicroBeads, human	Miltenyi Biotec	130-045-801
CellTrace CSFE dye	Thermo Fisher Scientific	C34554
CellTracker Deep Red	Thermo Fisher Scientific	C34565
Chromium Single Cell 3′ Library, Gel Bead & Multiplex Kit and Chip Kit, v2	10x Genomics	PN-120237
Chromium Single Cell A Chip Kit	10x Genomics	PN-120236
Chromium i7 Multiplex Kit	10x Genomics	PN-120262
CyTOF MaxPar X8 antibody labeling kits	Fluidigm	N/A
CyTOF EQ Four Element Calibration beads	Fluidigm	201078
CyTOF Barcode Perm Buffer	Fluidigm	201057
CyTOF Cell-ID Cisplatin	Fluidigm	201064
CyTOF Cell-ID Intercalator-Ir	Fluidigm	201192A
CyTOF Maxpar Cell Staining Buffer	Fluidigm	201068
CyTOF Palladium barcodes	Fluidigm	201060
Cytotoxicity Detection Kit	Roche Applied Science	11644793001
Fixable Viability Dye eFluor 780	eBioscience	65-0865-18
iScript cDNA synthesis kit	Bio-Rad	1708891
Pierce ECL Western Blotting Substrate	Thermo Fisher Scientific	32106
PureLink RNA Mini Kit	Thermo Fisher Scientific	12183018A
RNeasy Micro Kit	QIAGEN	74004
SuperScript III First Strand cDNA synthesis kit	Thermo Fisher Scientific	18080051
Deposited Data		
scRNA-sequencing raw and analyzed data CNV	This paper	ArrayExpress: E-MTAB-8119
Bulk RNA-sequencing data ALDH18A1 and SQLE silenced HUVEC	This paper	ArrayExpress: E-MTAB-8604
Proteomics raw and analyzed data ALDH18A1 and SQLE silenced HUVEC	This paper	PRIDE: PXD016678
Transcriptome data of murine lung TECs	(Goveia et al., 2020)	ArrayExpress: E-MTAB-7458
Transcriptome data of human cultured TECs	(Goveia et al., 2020)	ArrayExpress: E-MTAB-6308
Bulk RNA-seq dataset – renal cell carcinoma and colorectal cancer	EndoDB (Khan et al., 2019)	GEO: GSE77199
Bulk RNA-seq dataset – bladder cancer	EndoDB (Khan et al., 2019)	ArrayExpress: E-GEOD-41614
Bulk RNA-seq dataset – hepatocellular carcinoma	EndoDB (Khan et al., 2019)	ArrayExpress: E-GEOD-51401
Bulk RNA-seq dataset – medulloblastoma	N/A	ArrayExpress: E-GEOD-73753
Bulk RNA-seq dataset – B16 liver tumor dataset	EndoDB (Khan et al., 2019)	ArrayExpress: E-MTAB-4842

(*Continued on next page*)

Continued

REAGENT or RESOURCE	SOURCE	IDENTIFIER
Experimental Models: Cell Lines		
Human umbilical vein endothelial cells (HUVECs), primary; Approved by the Ethics Committee Research UZ/KU Leuven; approval number S57123	This paper	N/A
293T cells	ATCC	RRID: CVCL_0063
Lewis Lung Carcinoma cells	ATCC	RRID: CVCL_4358
Experimental Models: Organisms/Strains		
C57BL6/J mice, male	KU Leuven animal facility	N/A
C57BL6/J mice, male	Charles River	N/A
CD1 mice, male	KU Leuven animal facility	N/A
Oligonucleotides		
Human ALDH18A1 qRT-PCR primers	IDT Integrated DNA Technologies	NM_002860; Hs.PT.49a.38431
Human ALDH18A1 shRNA: CCGGCCTCAGTCGTACA CATGGAAACTCGAGTTTCCATGTGTACGACTGAGGTTTTTG	Sigma-Aldrich	TRCN0000064851; NM_002860.2-213s1c1
Human SQLE qRT-PCR primers	IDT Integrated DNA Technologies	NM_003129, Hs.PT.58.228785
Human SQLE shRNA: CCGGGCACCACAGTTTAAAGC AAATCTCGAGATTTGCTTTAAACTGTGGTGCTTTTTG	Sigma-Aldrich	TRCN0000046157; NM_003129.2-1154s1c1
Human HPRT qRT-PCR primers	IDT DNA Technologies	NM_000194; Hs.PT.58.2145446
Murine SQLE siRNA: 5′GGAAGAAAGGUGAC GGUCAUCGAGA3′	IDT Integrated DNA Technologies	Mm.Ri.Sqle.13.3
Murine SQLE qRT-PCR primers	IDT Integrated DNA Technologies	NM_009270; Mm.PT.58.5713471
Murine ALDH18A1 siRNA: 5′AGAUCUACAAU CAUGCUUAAAGGUCAAGCAUGAUUG3′	IDT Integrated DNA Technologies	NM_153554; Mm.Ri.Aldh18a1.13.2
Murine ALDH18A1 qRT-PCR primers	IDT Integrated DNA Technologies	NM_019698(2); Mm.PT.58.31161670
Murine HPRT qRT-PCR primers	IDT DNA Technologies	NM_013556; Mm.PT.42.12662529
RNAscope probe Mm-Nr2f2-C3	ACDBio	480301-C3
RNAscope Mm-Gja4	ACDBio	588591
RNAscope Probe 3-plex Positive Control Probe_Mm	ACDBio	320881
RNAscope Probe 3-plex Negative Control Probe	ACDBio	320871
Recombinant DNA		
pLKO-shRNA2 vector	Clontech	No. PT4052-5
pLKO.1-puro non-mammalian shRNA control	Sigma-Aldrich	SHC002V
Software and Algorithms		
R version 3.4.4 (2018-03-15), system: x86_64, mingw32, ui: RStudio (1.1.456), language: (EN), collate: English United States.1252	CRAN (R 3.4.4)	(CRAN, RRID: SCR_003005)
asinh (base R)	CRAN (R 3.4.4)	(CRAN, RRID: SCR_003005)
base (version 3.4.4)	Local	(CRAN, RRID: SCR_003005)
Cell Ranger	10x Genomics	(tenx, RRID: SCR_01695)
clusterProfiler; version 3.6.0	Bioconductor	(clusterProfiler, RRID: SCR_016884)
Dplyr; version *0.7.6*	CRAN (R 3.4.4)	(dplyr, RRID: SCR_016708)
edgeR; version *3.20.9*	Bioconductor	(edgeR, RRID: SCR_012802)
Fastcluster; version *1.1.25*	CRAN (R 3.4.4)	http://danifold.net/fastcluster.html
flashpcaR; version *2.0*	Local	https://github.com/gabraham/flashpca
ggplot2; version *3.0.0*	CRAN (R 3.4.4)	(ggplot2, RRID: SCR_014601)
GSVA; version *1.26.0*	Bioconductor	(Hänzelmann et al., 2013)
Heatmaply; version *0.15.2*	CRAN (R 3.4.4)	(CRAN, RRID: SCR_003005)
Limma; version *3.34.9*	Bioconductor	(LIMMA, RRID: SCR_010943)
Pathview; version *1.18.2*	Bioconductor	(Luo and Brouwer, 2013)

(*Continued on next page*)

Continued

REAGENT or RESOURCE	SOURCE	IDENTIFIER
Plotly; version *4.8.0.9000*	https://github.com/plotly/plotly.py	(Plotly, RRID: SCR_013991)
premessa R package	https://github.com/ParkerICI/premessa	N/A
Rtsne; version *0.13*	CRAN (R 3.4.4)	(Rtsne, RRID: SCR_016342)
SCENIC	(Aibar et al., 2017) https://aertslab.org/#scenic	N/A
scmap; version 1.1.5	Bioconductor	(Scmap, RRID: SCR_017338)
Scran; version *1.6.9*	Bioconductor	(scran, RRID: SCR_016944)
Seurat; version *2.3.2*	CRAN (R 3.4.4)	(Seurat, RRID: SCR_016341)
VennDiagram; version *1.6.20*	CRAN (R 3.4.4)	(VennDiagram, RRID: SCR_002414)
GraphPad Prism8, version 8.1.1	N/A	(GraphPad Prism, RRID: SCR_002798)
Fiji/ImageJ, 1.52n	https://fiji.sc	RRID: SCR_002285
FlowJo (version 8.8.6)	FlowJo, https://www.flowjo.com	(FlowJo, RRID: SCR_008520)
zFPKM	Bioconductor	https://bioconductor.org/packages/release/bioc/html/zFPKM.html
COBRA toolbox (version 3.0) for MATLAB R2018a	https://opencobra.github.io/cobratoolbox/stable/	N/A
Leiden algorithm (clustering coefficient)	Gephi 0.9.2	(Gephi, RRID: SCR_004293)
MaxQuant (version 1.6.0.16)	N/A	(MaxQuant, RRID: SCR_014485)
Xcalibur (version 4.0)	N/A	(Thermo Xcalibur, RRID: SCR_014593)
Other		
Antibiotic-antimycotic	Thermo Fisher Scientific	15240062
Bovine serum albumin	Sigma-Aldrich	A2058
Bovine serum albumin (UltraPure BSA)	Thermo Fisher Scientific	AM2616
Collagen type I	Merck Millipore	08-115
Collagenase I	Thermo Fisher Scientific	GIBCO 17100017
Collagenase II	Thermo Fisher Scientific	GIBCO 17101015
Collagenase type 4	Worthington Biochemical	LS004188
endoLysC	Wako	121-05063
Dispase	Thermo Fisher Scientific	171055-041
DMEM	Thermo Fisher Scientific	11965-084
DNase I	Sigma-Aldrich	D4527
ECGS (endothelial cell medium growth supplement mix)	Bio-Connect	PromoCell C-39216
ECGS/H (endothelial cell growth supplement/heparin)	Bio-Connect	PromoCell C-30140
EGM2 (Endothelial growth medium)	Bio-Connect	PromoCell C-22011
Fc receptor block TruStain FcX	BioLegend	422301
Fetal bovine serum (FBS)	Merck - Biochrom	S 0415
Fix/Perm buffer (eBiosciences intracellular fixation & permeabilization buffer set)	Thermo Fisher Scientific	88-8824-00
Gelatin from bovine skin	Sigma-Aldrich	G9391
Heparin (bullet of ECGS/H)	Bio-Connect	PromoCell C-30140
Medium 199, HEPES	Thermo Fisher Scientific	22340020
MEM NEAA	Thermo Fisher Scientific	11140035
MEM vitamin solution	Thermo Fisher Scientific	11120052
Penicillin/streptomycin	Thermo Fisher Scientific	15140122
Penicillin/streptomycin	Thermo Fisher Scientific	10378016
Phosphate buffered saline (PBS)	Thermo Fisher Scientific	14190094
Trypsin-EDTA (0.25%)	Thermo Fisher Scientific	25200056
Tween 80	Sigma-Aldrich	P1754

LEAD CONTACT AND MATERIALS AVAILABILITY

Correspondence and requests for materials should be addressed to the Lead Contact, Peter Carmeliet (peter.carmeliet@kuleuven.vib.be). This study did not generate new unique reagents.

EXPERIMENTAL MODEL AND SUBJECT DETAILS

Patient Material and Choroid EC Isolation

Human eyes from a post-mortem multiorgan donor were provided by the Biobank of UZ Leuven Hospital. Only leftover material after use for cornea transplantation was used. The donor had no eye pathology, the age and sex are unknown. The choroidal membranes were dissected and processed for scRNA-seq upon dissociating into single cell suspension in a digestion buffer (0.3% collagenase I, DNase I (7.5 μM) and dispase (2.5 U/mL) in DMEM supplemented with 1x sodium pyruvate, 1x MEM NEAAs, ECGF/Heparin, antibiotic/antimycotic (2x) and 1% penicillin/streptomycin (Thermo Fisher Scientific)) for 40 min at 37°C with manual pipetting every 10 min. The single cell suspension was enriched for ECs by MACS depletion of CD45 positive cells and subsequent enrichment of CD31 positive cells (Miltenyi Biotec).

Mice

Experiments were performed in 7 to 8 week-old male C57BL6/J mice (obtained from the KU Leuven animal facility or purchased from Charles River). Eight week-old male CD1 albino mice (obtained from the KU Leuven animal facility) were used for immunohistochemistry staining of healthy choroid. They had not been involved in other, previous procedures. Animals were maintained in individually ventilated cages in a room with controlled temperature (22 ± 2°C) and humidity under a 12 h light/12 h dark cycle and with food (ssniff R/M-H diet, V153x) and drink *ad libitum*. Animals were closely followed-up by the animal caretakers and the experimenters, with regular inspection by a veterinarian, as per the standard health and animal welfare procedures of the local animal facility. No statistical method was used to predetermine sample size. Animal housing and all experimental procedures were approved by the Institutional Animal Ethics Committee of the KU Leuven (Belgium) under protocol number P012/2014, P156/2015 and P035/2019.

Mouse Model of Choroidal Neovascularization

Choroidal neovascularization (CNV) was induced by laser burns as previously described with adaptations (Schoors et al., 2014) using a Purepoint Laser (Alcon, Fort Worth, USA). Ten or eight impacts (for choroidal endothelial cell isolation or immunostaining, respectively) rupturing the Bruch's membrane were made around the optical nerve using laser diameter 100 μm, power 0.320 W and exposure time 0.05 s in both eyes. At day 7, at the height of the angiogenic response (Lambert et al., 2013), mice were euthanized by cervical dislocation and the eyes were enucleated.

Murine Choroid Endothelial Cell Isolation

The RPE-choroid-sclera complex was dissected from enucleated eyes by peeling off the vitreous body and retina, pooled per group, and processed for scRNA-seq upon dissociating into single cell suspension in a digestion buffer (0.3% collagenase I, DNase I (7.5 μM) and dispase (2.5 U/mL) in DMEM supplemented with 1x sodium pyruvate, 1x MEM NEAAs, ECGF/Heparin, antibiotic/antimycotic (2x) and 1% penicillin/streptomycin) for 40 min at 37°C with manual pipetting every 10 min. The reaction was stopped with 10 mL of isolation buffer and the cell suspension was filtered through a 100 μm cell strainer. Single cell suspensions were enriched for ECs by MACS depletion of CD45 positive cells and subsequent enrichment of CD31 positive cells (Miltenyi Biotec). This procedure was repeated for 3 independent replicate experiments, and 3 additional experiments were performed to obtain reference samples of ECs isolated from healthy choroid of control mice without laser injury (referred to as healthy CECs; n = 2 eyes/mouse and n = 6 mice per experimental group).

Mouse model of Lewis Lung Carcinoma

Information about the animals and the orthotopic Lewis lung carcinoma (LLC) model are available elsewhere (Goveia et al., 2020). Briefly, the syngeneic LLC cells (ATCC) were injected orthotopically into the parenchyma of the right lung through the rib cage using a 30G needle (1×10^6 cells in 70 μl matrigel (BD Biosciences)). The animals were sacrificed on day 10 of the experiment and lungs were immediately processed for TEC and NEC isolation. Since both lungs become colonized by cancer cells in this orthotopic LLC model, even upon injection of cancer cells into a single lung, and since cancer cells in a tumor can affect peri-tumoral ECs, ECs from healthy non-tumor-bearing mice were used as controls.

Cell Lines and Primary Cell Culture

Human Umbilical Vein Endothelial Cells

Human umbilical vein endothelial cells (HUVECs) were freshly isolated from umbilical cords obtained from multiple donors of unknown sex (with approval from the Ethics Committee Research KU Leuven / UZ Leuven and informed consent obtained from all subjects) as previously described (Schoors et al., 2015). Briefly, the interior of the umbilical vein was rinsed with PBS containing antibiotic-antimycotic solution (Thermo Fisher Scientific) and injected with pre-heated collagenase I solution (0.2% collagenase type I in 0.9% NaCl, 2 mM $CaCl_2$, antibiotic-antimycotic). After no more than 13 min incubation, the collagenase suspension containing

endothelial cells (ECs) was collected, filtered through a 40 μm nylon cell strainer and spun down. The ECs were plated on 0.1% gelatin-coated dishes in M199 medium (1 mg/mL D-glucose) (Thermo Fisher Scientific) supplemented with 20% fetal bovine serum (FBS) (Merck-Biochrom), 2 mM L-glutamine (Thermo Fisher Scientific), Endothelial Cell Growth Supplement (ECGS)/ Heparin (PromoCell), 100 IU/mL penicillin and 100 μg/mL streptomycin (Thermo Fisher Scientific), and cultured until confluent in a 5% CO_2, 37°C incubator. The confluent cultures were split and replated in a 1:1 mixture of M199 and endothelial cell basal medium (EGM2) (PromoCell) supplemented with endothelial cell growth medium supplement pack (PromoCell) and further cultured in EGM2 medium. In all experiments, HUVECs were used as single-donor cultures and were used between passage (p) 2 and 4. Cultures were regularly tested for mycoplasma.

293T Cells

293T cells were purchased from ATCC and cultured in DMEM supplemented with 10% fetal bovine serum (FBS) (Merck-Biochrom), 2 mM L-glutamine (Thermo Fisher Scientific) and 100 IU/mL penicillin and 100 μg/mL streptomycin (Thermo Fisher Scientific).

METHOD DETAILS

In Vitro Functional Assays

Proliferation

EC proliferation was quantified by incubating cells for 2 h with 1 μCi/mL [^{3}H]-thymidine (Perkin Elmer). Thereafter, cells were fixed with 100% ethanol for 15 min at 4°C, precipitated with 10% TCA and lysed with 0.1 N NaOH. The amount of [^{3}H]-thymidine incorporated into DNA was measured by scintillation counting.

Scratch Wound Migration Assay

A scratch wound was applied on confluent EC monolayers (pre-treated overnight with 2 μg/mL Mitomycin C) using a 200 μL tip, 24 h after seeding (100,000 cells per well in 24-well plates). After scratch wounding and photography at time point 0 (T0), the cultures were further incubated in fully supplemented EGM2 medium for 18 h and photographed again (T18). Migration was measured with the *fiji/ImageJ* software package and is expressed as % wound closure (gap area at T0 minus gap area at T18 in % of gap area at T0).

Spheroid Capillary Sprouting Assay

ECs were incubated overnight in hanging drops in EGM2 medium containing methylcellulose (20 vol% of a 1.2% solution of methylcellulose 4000 cP) (Sigma-Aldrich) to form spheroids. When mitotic inactivation was required, Mitomycin C (1 μg/mL) was added to this medium. Spheroids were then embedded in collagen gel and cultured for 20 h to induce sprouting as described previously (De Bock et al., 2013). Cultures were fixed with 4% PFA at room temperature (RT) and imaged under bright field using a Motic AE 31 microscope (Motic Electric Group) or Leica DMI6000 microscope (Leica Microsystems). Analysis of the number of sprouts per spheroid and the total sprout length (cumulative length of primary sprouts and branches per spheroid) was done on phase contrast images using the *fiji* imaging software.

Mosaic Spheroid Capillary Sprouting Assay

Control and silenced ECs (lentiviral shRNA) were generated as described in the knockdown strategy section (see below), and fluorescently labeled with intracellular dyes. Control ECs were stained with the CellTracker Deep Red (Thermo Fisher Scientific) and SQLE or ALDH18A1 silenced ECs with the CellTrace CFSE dye (Thermo Fisher Scientific) according to the manufacturer's guidelines. Briefly, suspensions containing 125,000 control or silenced ECs were placed in a separate tube, spun down and the media were changed to EGM2 without growth factors and supplement during the incubation time with the dye (10 μM for CellTracker Deep Red, 50 μM of the CellTrace CFSE) for 30 min at RT in the dark. Excess full EGM2 was then added to the staining mix to remove remaining free dye in the solution, the cells were centrifuged and the supernatant was removed. Finally, control (Deep Red) and silenced (CFSE) cells were mixed at an equal ratio (1:1, 250,000 cells in total) and used for spheroid formation and sprouting as described above. Using a Leica DMI6000 microscope (Leica Microsystems) at least 10 spheroids were acquired per replicate and per condition. Using the *fiji/ImageJ* imaging software package, the contribution to the tip position of each sprout was quantified and represented as the percentage of green (CFSE) or red (Deep Red) stained ECs occupying the tip position.

Knockdown Strategy

In Vitro

To silence the expression of *ALDH18A1* or *SQLE*, gene-specific oligonucleotides (Key Resources Table) in the pLKO-shRNA2 vector (Clontech) were used. All constructs were sequence verified. Lentiviral particles were produced in 293T cells as previously described (Cantelmo et al., 2016). For lentiviral transduction, a MOI of 20-25 was used. Transductions were performed on day 0 in the evening, cells were refed with fresh medium on day 1 in the morning and experiments were performed from day 3 or 4 onward. Knockdown efficiency was monitored for each experiment either at the mRNA (qRT-PCR) or protein level or both and compared to expression in cells transduced with a negative control shRNA (Key Resources Table).

In vivo

To silence the expression of *ALDH18A1* or *SQLE* in the CNV model *in vivo*, siRNA duplexes directed against murine *Aldh18a1* or *Sqle*, or control siRNA (TriFECta Kit, IDT) were intravitreously injected (1 μg/eye) immediately after induction of the laser burns. At day 7 post-induction, the eyes were enucleated 10 min after retrobulbar injection with Fluorescein isothiocyanate (FITC)-conjugated dextran (Mr 2,000,000) (Sigma-Aldrich) and fixed in 2% paraformaldehyde. Choroids were dissected, flat-mounted (ProLong Gold

antifade reagent, Thermo Fisher Scientific) and imaged using a Leica TCS SPE confocal microscope (Leica Microsystems). Analysis of the neovascular area was performed with the Leica MM AF morphometric analysis software (Leica Microsystems) and expressed as the percentage of the FITC-dextran positive area in the total CNV lesion area. In order to check the genetic silencing in ECs upon *ALDH18A1* or *SQLE* siRNA treatment, choroidal ECs were isolated as specified above, and single cell suspensions were stained with viability dye-APC-Cy7 (Fixable Viability Dye eFluor 780, eBioscience), CD45-PeCy7 (eBioscience), CD31-FITC (eBioscience) and CD102-APC (Molecular Probes) antibodies at 4°C for 30 min, and viable, $CD45^-$, $CD31^+$, $CD102^+$ choroidal ECs were FACS sorted (BD FACSAria III). Cells were then processed for RNA extraction and qRT-PCR was performed.

Treatment with Inhibitor in the Murine Ocular Models

Choroidal Neovascularization Model

Male C57BL/6 mice with induced CNV were intravitreously injected with NB-598 (SQLE inhibitor, MedChemExpress) (250 μg/eye in 1 μl) or vehicle (0.05% DMSO, 1 μl) at day 1, 5, 8 and 11 post-laser induction. At 2 weeks after laser induction, mice were subjected to retrobulbar FITC-conjugated dextran injections, after which the mice were euthanized and eyes were enucleated. Eyes were fixed in 2% paraformaldehyde and choroids were dissected, flat-mounted and imaged using a Leica TCS SPE confocal microscope (Leica Microsystems). Neovascular morphometric analysis was performed as described above.

Corneal Cauterization Model

Corneal angiogenesis was induced by thermal cauterization as previously described (García-Caballero et al., 2019). After anesthetizing 8 week-old female mice with an intraperitoneal injection of ketamine (100 mg/kg body weight) and xylazine (10 mg/kg body weight), the local anesthetic (Unicaine 0.4%; Théa Pharma) was applied to the eye and the central cornea was thermally cauterized using an ophthalmic cautery device (Optemp II V; Alcon Surgical). Mice were daily treated with ophthalmic drops of NB-598 (250 μg/eye) or vehicle (0.05% DMSO) for 6 days, initiated the day after induction of the corneal injury. Mice were euthanized 7 days after cauterization, eyes were removed and corneas were dissected. Whole-mounted corneas were fixed in 70% ethanol for 1 h at RT and blocked with 3% BSA-3% Gloria milk (Nestlé) for 1 h. Corneas were then incubated overnight with a rat anti-mouse CD31 antibody (BD Biosciences), subsequently incubated with an AlexaFluor 546-conjugated goat anti-rat secondary antibody (Thermo Fisher Scientific) for 2 h, and flat-mounted on a microscopy slide with ProLong Gold antifade reagent (Thermo Fisher Scientific). Corneas were imaged using a Leica DMI6000 microscope (Leica Microsystems) and the blood vessel area was quantified ($CD31^+$ area as a percentage of the total corneal area).

Murine Choroid Immunostaining

Murine Eye Sections

Whole eyes were isolated and fixed in 2% paraformaldehyde for 2 h, embedded in paraffin blocks, sectioned and subjected to immunohistochemistry. Briefly, after permeabilization (2% trypsin in 0.1% CaCl2 for 7 min at 37°C), the samples were incubated overnight at 4°C with the specific primary antibody (anti-LXN, -APLNR, -PLGF, -CXCR4 and -SPARCL1) and an anti-CD31 antibody (BD Biosciences) for blood vessel detection. After incubation with the primary antibodies, samples were incubated overnight at 4°C with the appropriate secondary antibodies, stained with Hoechst and imaged with a Zeiss LSM 780 confocal microscope (Carl Zeiss) at 20x magnification (Fluar 20x/0.75).

Whole Mount Choroid

Eyes from CD1 albino mice were enucleated, fixed in 2% paraformaldehyde for 2 h, prior to choroid dissection. Thereafter, whole mount choroids were permeabilized and blocked (0.5% Triton, 0.01% sodium deoxycholate, 1% BSA, 2% serum in PBS) overnight at 4°C and subsequently incubated overnight at 4°C with the specific primary antibodies (anti-αSMA, -ELN, -SDF1/CXCL12, -VEGFR2, -SELP, -VWF) and with IsolectinB4-Alexa 488. Whole mount choroids were then incubated with the appropriate secondary antibodies and imaged with a Zeiss LSM 780 confocal microscope (Carl Zeiss) at 20x magnification (Fluar 20x/0.75).

RNA Isolation and Quantitative RT-PCR

RNA was collected and purified with the PureLink RNA Mini Kit (Thermo Fisher Scientific) or RNeasy Micro Kit (QIAGEN; for RNA isolation from choroidal ECs) and converted to cDNA using the iScript cDNA synthesis kit (Bio-Rad) or the SuperScript III First Strand cDNA synthesis kit (Thermo Fisher Scientific), respectively. RNA expression analysis was performed by Taqman quantitative RT-PCR (Thermo Fisher Scientific) as described using premade primer sets (Key Resources Table). For comparison of gene expression between conditions, mRNA levels (normalized to the housekeeping gene HPRT) were expressed relative to control conditions.

Single-cell Droplet-based RNA Sequencing

The single cell suspensions of freshly isolated choroidal ECs (MACS-bead enriched to 20%–30% as described above) were converted to barcoded scRNA-seq libraries using the Chromium Single Cell 3′ Library, Gel Bead & Multiplex Kit and Chip Kit (10x Genomics), aiming for 10,000 cells per library. Samples were processed using kits pertaining to v2 barcoding chemistry of 10x Genomics. Single samples were always processed in a single well of a PCR plate, allowing all cells from a sample to be treated with the same master mix and in the same reaction vessel. For each experiment, all samples (CNV-EC and CEC) were processed in parallel in the same thermal cycler. Libraries were sequenced on an Illumina HiSeq4000, and mapped to the human genome (build GRCh38) or to the mouse genome (build mm10) using CellRanger software (10x Genomics, version 2.1.1).

Single-cell Transcriptomics Analysis

Data from MACS-enriched samples were aggregated using Cell Ranger and data from the raw unfiltered matrix was further processed using R (version 3.4.4 - *Someone to Lean On*).

Quality Control and Data Normalization

The following quality control steps were applied: (i) genes expressed by < 50 cells or with a row mean of < 0.01 were not considered; (ii) cells that had either fewer than 201 (low quality cells) or over 6,000 expressed genes (possible doublets), or over 5% of unique molecular identifiers (UMIs) derived from the mitochondrial genome were removed. The data of the remaining cells were natural-log transformed using log1p and normalized using the *Seurat* package (Satija et al., 2015). Dataset-specific cut-off values and parameter settings are listed in Table S1.

In Silico EC Selection

After auto-scaling, the normalized data were first summarized by principal component analysis (PCA) using the *flashPCA* package, and the first 15 PCAs were visualized using t-Distributed Stochastic Neighbor Embedding (t-SNE, *Rtsne* package) with a perplexity value of 200 and a learning rate of 100. Graph-based clustering was performed to group cells according to their gene expression profiles as implemented in *Seurat*. Cell clusters were annotated based on canonical markers, including *Pecam1* and *Cdh5* (ECs), *Prox1* (lymphatic ECs), *Col1a1* (fibroblasts), *Ptprc* (leukocytes), *Pdgfrb* (pericytes) and *Acta2* (smooth muscle cells) to discriminate ECs from contaminating cells. All downstream analyses were performed on ECs only.

Batch Effect Correction

ECs from freshly-isolated murine samples were prospectively collected, resulting in several batches of sequencing data. We first analyzed each batch separately, and removed clusters expressing ambiguous marker genes (i.e., representing low quality cells, red blood cells, possible doublets, etc.). We then used a recently developed algorithm, *mnnCorrect* available from the *scran* package (Haghverdi et al., 2018), for batch effect correction. The optimal neighborhood size, k, was empirically defined as 50 after optimizing over a range of 10-300 for both human and murine datasets. Because scRNA-seq data were batch corrected, gene expression patterns are presented on semiquantitative scales.

Feature Selection and Dimensionality Reduction

After *in silico* EC selection and batch correction for joint analysis, we identified genes with high variability using the Seurat *FindVariableGenes* function. This function calculates the mean expression and dispersion for each gene, then groups genes into bins (of size 20) by their mean expression and identifies any gene for which the z-score calculated from the dispersion exceeds a pre-defined cut-off. For most experiments, we used a cut-off of z = 0.25 and mean expression in the range 0.00125 to 8, all other parameters were default (see Table S1 for parameter settings for each analysis). The normalized data were auto-scaled and principal component analysis was performed on variable genes, followed by t-SNE to construct a two-dimensional representation of the data. This representation was only used to visualize the data.

EC Cluster Identification

To estimate the number of distinct phenotypes in batch corrected data, we color-coded t-SNE plots for each of the ~14,000 detected genes using an in-house developed R/Shiny-based web tool and identified clusters of cells with discriminating gene expression patterns. To unbiasedly group ECs, we performed PCA on highly variable genes, and used graph-based clustering as implemented in the *FindClusters* function of the *Seurat* package (Satija et al., 2015). Cluster results were visualized using t-SNE to verify that all visually identified clusters were captured and not under-partitioned. Over-partitioned clusters that represent the same biological phenotype were merged into a single cluster. Details of clustering parameters are listed in Table S1. Given the large number of sequenced choroid ECs, subclustering was performed on arterial, venous and CNV clusters using the method described above (Table S1 for parameter settings).

Marker Gene Analysis

We used a two-step approach to obtain ranked marker gene lists for each cluster. As a first criterion, marker genes for a given cluster should have the highest expression in that cluster compared to all other clusters and are therefore uniquely assigned to one cluster. Second, we ranked marker genes using a product-based meta-analysis (Hong et al., 2006). Briefly, we performed pairwise differential analysis of all clusters against all other clusters separately and ranked the results of each pairwise comparison by $\log_2$ fold change. The most upregulated genes received the lowest rank number (top ranking marker genes) and the most downregulated genes received the highest rank number. For each cluster, we combined the rank numbers for all genes in all pairwise comparisons by calculating their product to obtain a final list of ranked marker genes for each cluster.

Cluster Annotation

We annotated clusters based on literature-curated marker genes of canonical artery, capillary, vein, lymphatic, proliferating and tip ECs. In case of an entirely unknown phenotype or unknown sublineages of a canonical phenotype, which could not be annotated based on canonical marker genes or gene sets, we used a three-step approach to identify a putative biological function. First, we

searched through the top 50 ranking list of markers for a coherent set of genes involved in similar biological processes. Second, if we identified a putative signature (e.g., basement remodeling, etc.), we determined whether other genes associated with such a signature were also highest expressed in this phenotype. Cells that could not be unambiguously assigned to a biologically meaningful phenotype might represent low quality cells or doublets and were excluded from the analysis.

Gene Set Variation Analysis

Gene set variation analysis (GSVA) as implemented in the GSVA R-package (version 1.26.0) was performed using default settings (Hänzelmann et al., 2013).

Evaluation of Dissociation Artifacts

We performed gene set variation analysis to determine which individual cells strongly expressed a recently published dissociation gene signature, consisting mainly of immediate-early and other stress response genes (van den Brink et al., 2017).

Heatmap Analysis

All heatmaps are based on cluster-averaged gene expression to account for cell-to-cell transcriptomic stochastics. Data was auto-scaled for visualization. Heatmaps were produced using the *heatmaply* package (version 0.15.2). The datamatrix for each heatmap can be downloaded from the accompanying web tool (see Data Resources below).

Trajectory Inference

We used the *SCORPIUS* package (version 1.0.2) to place cells onto pseudotime trajectories (Cannoodt et al., 2016). *SCORPIUS* assumes that a given dataset contains the genome-wide expression profiles of hundreds to thousands of cells, which were uniformly sampled from a linear dynamic process. Using this method, an initial trajectory is constructed by clustering the data with k-means clustering and finding the shortest path through the cluster centers. This initial trajectory is subsequently refined in an iterative way using the principal curves algorithm. The individual cells can then be ordered by projecting the n-dimensional points onto the trajectory.

We performed feature selection by selecting the top 20 marker genes for each cluster included in the pseudotime analysis. Dimensionality reduction was performed using the *reduce_dimensionality* function (we used 10 dimensions, all other parameters were default). Individual ECs from each CNV cluster were subsequently placed onto linear pseudotime using the *infer_trajectory* function of the *SCORPIUS* package using default settings. Proliferating cells express a highly distinct signature consisting almost entirely of cell cycle associated genes and could therefore not be placed on the differentiation trajectory. A similar analysis was performed for TECs.

Jaccard Similarity Analysis

To assess conservation of cell phenotypes across models, we calculated similarity of marker gene sets using pairwise Jaccard similarity coefficients for all clusters against all other clusters. The Jaccard similarity coefficient is defined as the size of the intersection divided by the size of the union of sets:

$$J(A,B) = \frac{|A \cap B|}{|A \cup B|} = \frac{|A \cap B|}{|A| + |B| - |A \cap B|},$$

where J is the Jaccard index and A and B are two sets of marker genes (Levandowsky and Winter, 1971).

Gene Set Enrichment Analysis

We used gene set enrichment analysis (GSEA) as implemented in the *clusterProfiler* package (version 3.6.0) to compare gene expression signatures of TEC versus NEC and CNV-EC versus CEC samples (Yu et al., 2012). Gene set analysis was performed using a set of vascular related and metabolic gene sets selected from the Molecular Signatures Database (MSigDB version 5.2 downloaded from http://bioinf.wehi.edu.au/software/MSigDB/), a collection of expert annotated gene sets. GSEA scores were calculated for sets with a minimum of 10 detected genes, all other parameters were default.

Metabolic Gene Expression Analysis and Pathway Mapping

For metabolic gene expression, all analyses were performed on a data matrix filtered for the subset of metabolic genes, as described previously (Cantelmo et al., 2016). Consistent with previous bulk analyses in pathological ECs (Cantelmo et al., 2016), we detected 1,255 and 1,187 metabolic genes in CNV-ECs and TECs, respectively. Semiquantitative pathway mapping was performed using the *pathview* package (version 1.18.2) using a color-scale range of batch corrected gene expression values of −0.01 to 0.01 and 5 bins (Luo and Brouwer, 2013). Genes with a batch corrected expression level below 0.005 in the bulk population were considered too lowly expressed and were excluded from the pathway map. To clarify visualization, the default KEGG pathways were redrawn as presented in Figures 4B and S4A. Pathway mapping using non-batch corrected data showed similar results (data not shown).

Cell Cycle Pseudotime Analysis

We previously identified a distinctive cluster of proliferating ECs in cultured human TECs (Goveia et al., 2020). Reanalysis of this dataset revealed that proliferating ECs organized in a circular geometry on t-SNE that upregulated known cell cycle restricted genes. Color-coding t-SNE plots for cell cycle phase-specific gene sets showed that proliferating ECs in the circular pattern were sequentially ordered based on their progression through the cell cycle.

To computationally reconstruct cell cycle pseudotime, we performed a spatial sign transformation on the first and second t-SNE dimension coordinates to project all cycling cells in our cultured sample onto the unit circle, and defined cell cycle pseudotime for each cell as the arc angle theta (θ) from an arbitrary point (t = 0) on the cycle. Next, we used local polynomial regression to model pseudo-temporal gene expression and confirmed the known cell cycle-related periodicity of cyclin gene expression (Santos et al., 2015; Whitfield et al., 2002). We assigned cell cycle phases based on the periodic expression of cyclins and expressed cell cycle pseudotime as percentage of the cell cycle (where 0% approximately coincides with cytokinesis). Finally, we used a previously validated standard deviation based method to obtain a ranked list of periodically expressed genes (de Lichtenberg et al., 2005).

Development of a Multivariate Model to Predict Cell Cycle Pseudotime

As an extension of previous reports demonstrating the general applicability of *in vitro* trained machine models to assign cell cycle phases to individual cells in a variety of cell types (Scialdone et al., 2015), we developed a prediction model to reconstruct continuous cell cycle pseudotime in proliferating murine CNV-ECs and TECs based on periodically expressed genes identified in cultured cells. We first used the human cultured TEC dataset to reconstruct ten cell cycle gene sets, each consisting of genes with peak expression in distinct phases of the cell cycle (i.e., genes that peak between 0%–10%, 10%–20%, etc. pseudotime). Second, we trained a multivariate model to predict the x- and y-coordinates of individual cells on the unit circle, and calculated pseudotime using the inverse tangent of spatial sign transformed predictions. Pseudo-temporal gene expression was modeled using local polynomial regression.

Pathway and Transcription Factor Activity Analysis

Gene set variation analysis (GSVA) (Hänzelmann et al., 2013) was used to convert the gene-by-cell matrix into a gene set-by-cell matrix. GSVA scores were only calculated for gene sets with a minimum of five detected genes, all other parameters were default. SCENIC transcription factor analysis (Aibar et al., 2017) was run as described previously, using the 20,000 motifs database for RcisTarget and GRNboost (*SCENIC* version 0.1.5, which corresponds to RcisTarget 0.99.0 and AUCell 0.99.5; with RcisTarget.hg19.motifDatabases.20k). The input matrix was the normalized expression matrix output, from which 14,917 genes passed the filtering.

Bulk RNA-sequencing Analysis

RNA was extracted from control, SQLE and ALDH18A1 silenced cells and purified with the PureLink RNA Mini Kit (Thermo Fisher Scientific). Starting from 1 μg total RNA, poly-adenylated fragments were isolated, reverse transcribed and converted into indexed sequencing libraries using the KAPA stranded mRNA-seq kit (Sopachem). The first 50 bases of these libraries were sequenced on a HiSeq 2500 system (Illumina). The raw sequenced reads were mapped to the human reference transcriptome and genome (build GRCh38) using the Bowtie TopHat pipeline (Langmead and Salzberg, 2012). Mapped reads were assigned to Ensemble gene IDs by HTSeq. Differentially expressed genes and their false discovery rate (FDR) corrected p values were identified by the *Limma* package (Ritchie et al., 2015).

Proteomics Sample Preparation

Control, SQLE and ALDH18A1 silenced cells were collected and frozen as a dry pellet before extraction in 300 μL of a 50:30:20 (methanol: acetonitrile: 20 mM Tris, pH 9.3) extraction buffer. Samples were then centrifuged for 5 min at 15,000 rcf at 4°C and the supernatant was discarded. The resulting protein pellet was re-dissolved in 50 μl 8 M urea, 20 mM HEPES pH 8.0 and proteins were reduced by addition of 15 mM DTT and incubation for 30 min at 55°C. Proteins were then alkylated by incubation with 30 mM iodoacetamide for 15 min at RT in the dark. The samples were diluted by addition of 20 mM HEPES pH 8.0 to reach a urea concentration of 4 M; then, the proteins were digested with 0.125 μg endoLysC (Wako 1/250, w/w) for 4 h at RT. Next, all samples were further diluted by addition of 20 mM HEPES pH 8.0 to a final urea concentration of 2 M and the proteins were digested with 0.125 μg trypsin (Promega) (1/100, w/w) overnight at 37°C. The resulting peptides were then purified on OMIX C18 tips (Agilent), dried completely by vacuum drying and stored at −20°C until LC-MS/MS analysis.

Proteomics LC-MS/MS and Data Analysis

Peptides from each sample were re-dissolved in 20 μL loading solvent A (0.1% TFA in water/acetonitrile (98 : 2, v/v)) of which 10 μL was injected for LC-MS/MS analysis on an Ultimate 3000 RSLCnano system (Thermo Fisher Scientific) in-line connected to a Q Exactive HF mass spectrometer (Thermo Fisher Scientific) equipped with a Nanospray Flex Ion source (Thermo Fisher Scientific). Trapping was performed at 10 μl/min for 4 min in solvent A on a home-made 100 μm internal diameter (I.D.) × 20 mm trapping column (5 μm beads, C18 Reprosil-HD, Dr Maisch) and peptides were separated on a reverse-phase column (made in-house, 75 μm I.D. × 400 mm, 1.9 μm beads C18 Reprosil-HD, Dr Maisch). The peptides were eluted by a non-linear increase from 2% to 56% MS solvent B (0.1% FA in water/acetonitrile (2 : 8, v/v)) over 140 min at a constant flow rate of 250 nL/min. The column temperature was kept constant at 50°C (CoControl 3.3.05, Sonation).

The mass spectrometer was operated in data-dependent mode, automatically switching between MS and MS/MS acquisition for the 16 most abundant ion peaks per MS spectrum. Full-scan MS spectra (375 to 1500 m/z) were acquired at a resolution of 60,000 in the Orbitrap analyzer after accumulation to a target value of 3,000,000. The 16 most intense ions above a threshold value of 13,000 were isolated (window of 1.5 Th) for fragmentation at a normalized collision energy of 28% after filling the trap at a target value of 100,000 for maximum 80 ms. MS/MS spectra (200 to 2,000 m/z) were acquired at a resolution of 15,000 in the orbitrap analyzer. The S-lens RF level was set at 55, and we excluded precursor ions with single and unassigned charge states from fragmentation selection.

Data analysis was performed with MaxQuant (version 1.6.0.16) (Cox and Mann, 2008) using the Andromeda search engine with default search settings, including a false discovery rate set at 1% on peptide spectrum match (PSM), peptide and protein level. The spectra were searched against the human proteins in the UniProt/Swiss-Prot database (database release version of September 2017 containing 20,237 human protein entries, downloaded from https://www.uniprot.org/). The mass tolerances for precursor and fragment ions were set to 4.5 and 20 ppm, respectively, during the main search. Enzyme specificity was set as carboxy-terminal to arginine and lysine (trypsin), also allowing cleavage at arginine/lysine–proline bonds with a maximum of two missed cleavages. Carbamidomethylation of cysteine residues was set as a fixed modification and variable modifications were set to oxidation of methionine (to sulfoxides) and acetylation of protein amino-termini. Proteins were quantified by the MaxLFQ algorithm integrated in the MaxQuant software. Only proteins with at least one unique or razor peptide were retained for identification, while a minimum ratio count of two was required for quantification. Matching between runs was enabled, with a matching time window of 2 min and an alignment time window of 20 min.

Further data analysis was performed in R after loading the proteinGroups results files from MaxQuant. Proteins with less than 20% valid values were removed, and missing values were imputed using minimum values. Differentially expressed proteins and their false discovery rate (FDR) corrected p values were identified by the *Limma* package (Ritchie et al., 2015), non-corrected p values are reported for targeted analysis of collagen modification enzymes.

Metabolomics and Data Analysis

Liquid Chromatography Mass Spectrometry

Control, SQLE^{KD} and ALDH18A1^{KD} HUVECs grown in a 6-well plate were washed with ice cold 0.9% NaCl solution and scraped into an extraction buffer (80% LC-MS grade methanol in water). Next, proteins were pelleted by centrifugation at 20,000 g for 15 min at 4°C. Part of the supernatant was transferred to LC-MS vials. The cell pellet was lysed in 200 mM NaOH for 20 min at 95°C. After centrifugation at 1,000 g for 10 min, protein levels were measured by BCA for normalization purposes.

Untargeted Measurements

Untargeted measurements were performed using the Vanquish UHPL system (Thermo Fisher Scientific) in-line connected to an Orbitrap Fusion Lumos Tribrid mass spectrometer (Thermo Fisher Scientific). Five μl of sample was injected and loaded onto a Hilicon iHILIC-Fusion(P) stainless steel column (Achrom, 150 × 2.1 mm 1.8 μm 100 Å). A linear gradient was carried out starting with 90% solvent A (LC-MS grade acetonitrile) and 10% solvent B (10 mM ammoniumacetate pH 9.3). From 2 to 20 min the gradient changed to 80% B and was kept at 80% until 23 min. Next a decrease to 40% B was carried out to 25 min, further decreasing to 10% B at 27 min. Finally 10% B was maintained until 35 min. The solvent was used at a flow rate of 200 μl/min, the column temperature was kept constant at 25°C. The mass spectrometer operated in negative ion mode, settings of the HESI probe were as follows: sheath gas flow rate at 34, auxiliary gas flow rate at 5 (at a temperature of 275°C). Spray voltage was set at 2.5 kV, temperature of the ion transfer tube at 300°C and S-lens RF level at 50. A full scan (resolution of 120,000 and scan range of m/z 50-750) was applied.

Targeted Measurements

Targeted measurements of proline and energy balance ([ATP + ½ ADP]/[ATP+ADP+AMP]) were performed using a Dionex UltiMate 3000 LC System (Thermo Fisher Scientific) in-line connected to a Q-Exactive Orbitrap mass spectrometer (Thermo Fisher Scientific). 10 μl of the sample extracts (collected in 80% LC-MS grade methanol in water as described above) were separated on an Acquity HSS T3 UPLC column (Waters Corp, 2.1 mm x 150 mm, 1.8 μm particle size) using an Ultimate 3000 HPLC (Dionex, Thermo Fisher Scientific). Column temperature was held at 40°C throughout the analysis. Elution of metabolites was performed using a quaternary solvent system consisting of solvent A (10 mM Tributylamine, 15 mM acetic acid 5% methanol in water) and solvent B (100% methanol). The flow rate is kept constant at 250 μl/min and the following linear gradient is applied: at 0 min 0% B, from 2 to 7 min an increase to 37% B is accomplished; from 7 min to 14 min an increase to 41% B is carried out, from 14 to 26 min the gradient increases to 100% B and is maintained until 30 min. At 31 min the gradient progressively decreases to 0% B and lasts until 40 min. The data was then collected in "centroid data acquisition" mode, with negative electron spray ionisation over a mass range of 70 – 1050 m/z and an extra filter of 300-850m850 m/z starting from the 8th min. Both were at a mass resolution of 70,000 (at m/z 200). The detector was an Orbitrap Qexactive (Thermo Fisher Scientific). Source settings were the following: sheath gas flow rate at 50, aux gas flow rate at 10, spray voltage at 4 kV, capillary temperature at 350°C and the S-lens RF level was set at 60.

Data Processing

Mass spectrometry files were converted to the mzXML format using msConvert available from the proteowizard toolkit (Chambers et al., 2012). All downstream analyses were performed in R. For targeted measurements, analysis was performed using the *Quan* software (Thermo Fisher Scientific, *Xcalibur* version 4.0) and manually verified.

Hydroxyproline Content

Hydroxyproline content was quantified according to Creemers et al. (1997). Briefly, cells were scraped and hydrolyzed for 3.5 h at 135°C in 6 N HCl. Samples were vacuum-evaporated and dissolved in demineralized water. Hydroxyproline residues were oxidized by adding chloramine T reagent (chloramine T in 50% n-propanol; all Sigma-Aldrich), followed by the addition of Ehrlich's aldehyde reagent (mixture of p-dimethylaminobenzaldehyde, n-propanol and perchloric acid; all Sigma-Aldrich) and incubation of the samples at 65°C for chromophore development. A hydroxyproline standard curve was used to calculate the absolute amount of hydroxyproline per sample, which was finally normalized to protein content after BCA measurement.

Meta-analysis of Transcriptomics Data

We performed a differential gene expression meta-analysis using previously published tumor ECs (TEC) versus normal ECs (NEC) transcriptomics. Briefly, we screened the EndoDB database for relevant studies and identified three studies comprising nine distinct TEC versus NEC datasets of eight tumor types (Khan et al., 2019). We performed pairwise, TEC versus NEC, differential expression analysis for each dataset independently as described previously (Bruning et al., 2018; Cantelmo et al., 2016). Differentially expressed genes and their false discovery rate (FDR) corrected p values were identified by the *Limma* package (Ritchie et al., 2015). We ranked genes in each dataset by fold change; genes upregulated in TECs received the lowest rank, downregulated genes the highest rank. We combined the rank numbers for all genes using a product-based meta-analysis (Hong et al., 2006). For visualization purposes only, we plotted the scaled median ranks.

RNAscope *In Situ* Hybridization and Quantification

Formalin-fixed paraffin-embedded whole murine eyes were sectioned and subjected to RNAscope *in situ* hybridization using the RNAscope Multiplex Fluorescent v2 assay (ACDBio) according to the manufacturer's instructions (Pretreatment and RNAscope Multiplex Fluorescent v2 Assay according to protocol 323100-USM). Briefly, after deparaffinization, the slides were incubated with hydrogen peroxide for 10 min at RT. After several washing steps, manual target retrieval was performed followed by incubation with Protease Plus before proceeding to the RNAscope Multiplex Fluorescent v2 protocol. Hybridization was performed with the RNAscope probes Mm-Nr2f2-C3 (480301-C3), Mm-Gja4 (588591), and RNAscope Probe 3-plex Positive Control Probe_Mm (320881) and RNAscope Probe 3-plex Negative Control Probe (320871). Slides were then processed according to the RNAscope Multiplex Fluorescent v2 protocol (Hybridization, Amplification, and Signal Development), prior to immunohistochemical staining for CD105 (Goat CD105, R&D Systems, AF1320, 1:200). Images were acquired using a Zeiss LSM 780 confocal microscope (Carl Zeiss). For quantification, the *in situ* hybridization images were first converted to a thresholded image and number of particles per $CD105^+$ cell was counted using a circularity of 0.00 – 1.00, and a size pixel between 0 – ∞. Doublets and triplets were split by considering signal over the average size of a dot. Results are depicted as number of dots per cell as estimated by counting nuclei (stained with Hoechst). Depicted data are representative eye sections of n = 3 CNV-induced mice.

Cytometry by Time of Flight Mass Cytometry (CyTOF)

Custom conjugated antibodies were generated using MaxPar X8 antibody labeling kits as per the manufacturer's instructions (Fluidigm). Single cell suspensions of freshly isolated CECs and CNV-ECs were washed twice in PBS followed by incubation with 0.5 mM Cell-ID Cisplatin (Fluidigm) for 3 min at RT. Reactions were quenched with 5 mL Cell Staining Buffer (Fluidigm), washed and fixed in 2% paraformaldehyde for 20 min at RT. Cells were then washed and permeabilized with freshly prepared 1X Barcode Perm Buffer in PBS (Fluidigm), followed by incubation with Palladium barcodes (Fluidigm) for 20 min at RT. Samples were subsequently washed with Cell Staining Buffer, re-suspended with Fc receptor block for 5 min (TruStain FcX, BioLegend) and stained with a cocktail of surface staining antibodies for 1 h at RT under constant rotation. Following washes with Cell Staining Buffer and PBS, samples were fixed for 30 min in Fix/Perm buffer (eBiosciences). After 2 washes with freshly prepared 1X Perm Buffer (eBiosciences), cells were stained with a cocktail of intracellular staining antibodies for 1 h at RT under constant rotation. Cells were then washed twice in 1X Perm Buffer and once in PBS, followed by incubation with 1.6% paraformaldehyde and 0.5 μM Intercalator-Ir (Fluidigm) for 1 h at RT. After multiple washes with Cell Staining Buffer, PBS and finally ultrapure water, EQ Four Element Calibration beads (Fluidigm) were added 1:10 to each sample followed by analysis on a Helios instrument (Fluidigm) at an event rate of 150–200 cells per second.

CyTOF Data Analysis

Bead-normalized samples were debarcoded using the *premessa* R package (minimum separation 0.3, maximum Mahalanobis distance 30). The viable fraction (DNA^+, $Cisplatin^-$) of debarcoded single cells was then selected using FlowJo, and viable cells were sequentially gated on $CD45^-$/$PDGFRB^-$/$COL1A1^-$/$ACTA2^-$ /$PECAM1^+$/$CDH5^+$ endothelial cells. Protein expression matrices were generated using R, and arcsin transformation was applied to the marker intensities. Dimensionality reduction of the data was performed based on the expression of the remaining markers using the t-SNE algorithm, with a perplexity value of 200 and a learning rate of 100.

Curation of a GEM Model

The Recon 1 generic human reconstruction (Duarte et al., 2007) was verified for mass and stoichiometry imbalance, presence of dead-end metabolites and blocked reactions using the *verifyModel* function implemented in COBRA toolbox v3.0 for MATLAB R2018a (Heirendt et al., 2019). The model was subsequently manually curated by: (i) removing reactions and metabolites without

metabolic fates (no upstream/downstream reactions); (ii) addition of transporters between intra- and extracellular compartments; and (iii) adding reactions belonging to fatty acid oxidation, citric acid cycle, branched chain amino acid, cholesterol, glycine, serine and threonine metabolism from Recon 2.2 (Swainston et al., 2016). The curated model contains 3,894 reactions (2,201 gene-associated; 1,693 non-gene associated) and 2,691 metabolites belonging to 98 pathway categories across seven subcellular compartments (cytoplasm, endoplasmic reticulum, mitochondria, lysosome, Golgi, nucleus, peroxisome).

Development of an EC-tailored GEM

We tailored the curated model to a generic EC-specific GEM using transcript abundance (in fragments per kilobase of transcript per million mapped reads, FPKM) of genes expressed in human umbilical vein ECs (HUVECs) in two independent RNA-sequencing studies (GSE76743, E-MTAB-4897). The FPKM abundance of each gene in each sample was z-score normalized (zFPKM) using the *zFPKM* package (Hart et al., 2013) to make samples within the same study comparable. These genes along with the zFPKM expression values (averaged between samples) were mapped onto the reactions present within the curated Recon 1.0 model. If a reaction was associated with multiple genes (enzymes), the average of the zFPKM of all the associated genes was considered as the transcriptional expression weight for that reaction.

Using the GIMME algorithm (Becker and Palsson, 2008), reactions with an average expression (zFPKM) less than −3 were minimized in the model (Hart et al., 2013), while keeping the biomass objective above 90% of its optimal value. To avoid inappropriate exclusion of alternative pathways after integration of RNA-sequencing data, we defined a superset of reactions (optimal flux solutions) that are active when optimizing the model for at least one of 988 flux profiles (derived from separately optimizing for the production of 38 biomass precursors (Table S5), while providing each of 26 metabolites (20 amino acids, L-cystine, inositol, triacylglycerol, glucose, thymidine, palmitate) as separate inputs). We then assessed for each reaction that was constrained to zero by GIMME, whether it was an element of the optimal superset. Reactions that belonged to this optimal superset were re-assigned as active (constrained to default bounds provided by the COBRA toolbox 3.0) and retained within the model.

Development of EC Tailored Objective Functions

Two EC-specific objective functions for biomass production and collagen synthesis were defined using available biochemical compositions of biomass precursors in ECs reported in the literature or measured in-house (Table S5). As there is no dry weight (DW) composition available for ECs, the overall weight percentage and percentage composition of proteins (78%), DNA (1%), RNA (4%) and lipids (17%) of a generic human cell was considered for the formulation of the biomass function (Shlomi et al., 2011). The fractional contribution of the nucleotide precursors for DNA and RNA were obtained from previously formulated biomass reactions in other human metabolic reconstructions (Shlomi et al., 2011). The molar contribution of amino acids was calculated from the total available amino acid pool measured in control bovine aortic ECs (Baydoun et al., 1990). Molar fractions of lipids and cholesterol were obtained from 2 separate studies (Murphy et al., 1992; Rastogi and Nordøy, 1980). Molar fractions were used to calculate the millimolar contributions of biomass precursor metabolites in mmol/gDW of a cell (Shlomi et al., 2011).

The flux associated with the biomass reaction represents the specific growth rate of ECs. Constraints on the biomass were set using *Metabotools* (Aurich et al., 2016), as implemented in COBRA toolbox v3.0 incorporating the mean HUVEC doubling time of 36 h with a 20% tolerance in the rate. A collagen synthesis reaction was formulated by considering the biochemical compositions of the twenty amino acids and the addition of fractional composition of 4-hydroxyproline as measured in our study. For this, the composition of 4-hydroxyproline measured in-house (μg/μg protein in 250 μl for 250,000 cells as shown in Figure S6F) was converted to mmol/gDW of a cell. The growth associated energy requirement was considered to be 24 mmol ATP/gDW (Shlomi et al., 2011).

Development of an Angiogenic CEC-GEM Model

The EC-GEM model was refined to model CNV-EC functions in three steps. First, microarray data of quiescent and proliferating HUVECs (GEO: GSE89174) were used to derive an angiogenic EC-GEM. Specifically, genes that were downregulated (log fold change < −1) in proliferating HUVECs, were mapped to the EC-GEM model and the associated reactions were constrained to zero after checking for their essentiality to maximize the two objective functions using flux balance analysis (FBA) (O'Brien et al., 2015). Reactions that were essential for the objective were retained. Second, the EC-GEM was refined to impose CEC-specific constraints. Reactions corresponding to the differentially regulated genes in the CECs as compared to the HUVECs (bulk RNA-sequencing study, GEO: GSE20986) were constrained to zero if the gene was downregulated in CECs (log fold change < −1.5) after checking for their essentiality toward biomass or unconstrained if the gene was upregulated in CECs (log fold change > 1.5) in the proliferating model. By doing so, 26 reactions were constrained to zero and 36 reactions were re-activated. Third, the CEC-GEM was further refined by eliminating reactions corresponding to genes with undetectable transcripts (row means of all ECs < 0.01) in scRNA-seq data of human CECs.

To obtain a functional model, we checked the absolute requirement of each reaction toward biomass production before elimination and retained them if essential for maximizing biomass. Thereby, 1,593 reactions were assigned inactive to obtain a proliferating CEC-GEM flux profile for biomass synthesis. The same procedure was repeated for the collagen synthesis function, resulting in the elimination of 2,037 reactions.

The proliferating GEM was further tailored based on available flux data in ECs. Constraints were refined to identify a flux space that simultaneously utilizes fatty acid oxidation for dNTP synthesis, and maintains a higher requirement of aspartate in cytoplasm than mitochondrion, lactate production and an active TCA cycle as previously reported (Fitzgerald et al., 2018; Schoors et al., 2015).

To do this, the extracellular uptake rates of metabolites in the CEC-GEM were constrained using the biochemical compositions of the M199 medium within COBRA toolbox v3.0 (Aurich et al., 2016), and we performed flux variability analysis (FVA) (Mahadevan and Schilling, 2003) and random sampling of flux distributions using the CHRR algorithm (Haraldsdóttir et al., 2017), to refine constraints. To ensure compartmentalization of glucose for ATP production via glycolysis, while diverting fatty acids toward mitochondrial acetyl-coA production via fatty acid oxidation, an arbitrary reduction in pyruvate carboxylase flux and an imbalance in the malate-aspartate shuttle was incorporated within the model.

Prediction of Essential Genes in the Angiogenic CEC Model

The refined proliferating CEC model was subsequently used for prediction of essential reactions. We identified model reactions as essential if a given reaction is crucial for independently optimizing the two objective functions, the least variable across alternate optimal flux solutions and coupled with large number of other reactions within the network. To identify reactions with these properties, we employed four separate flux-based approaches: (i) flux sampling (fs): Since there are many alternate biochemical pathways that can provide the same optimal biomass, CEC-GEMs were sampled to obtain 100,000 flux profiles considering a uniform sampling distribution. Sampling was performed using the CHRR algorithm (Haraldsdóttir et al., 2017). The relative flux variance of each reaction (variance of flux associated with a reaction normalized to the most varying reaction) was calculated. By this method, a reaction was shortlisted to be important if it was the least varying across the generated samples (relative variance < 0.1); (ii) flux variability analysis (FVA): Given the CEC specific constraints, the minimum and maximum fluxes through a reaction were estimated using FVA, while considering solutions that produce at least 90% of the biomass reaction. The absolute difference between the minimal and maximal flux for each reaction represents the range of the flux activity of that reaction. By this method, a reaction was shortlisted to be important if the absolute flux difference was < 1% of the maximum flux difference associated with a reaction in the network; (iii) reaction essentiality (RE): The "wild-type" solution in the CEC-GEMs that maximizes biomass was calculated using a combination of flux balance analysis (FBA) and cycleFreeFlux (to remove stoichiometrically balanced cycles) algorithms (Desouki et al., 2015). A reaction knockout analysis was performed in the CEC-GEMs to test the effect of perturbation on biomass synthesis. A reaction was deemed to be essential, when the *in silico* knockout of a reaction (flux through that reaction constrained to zero) leads to a 90% reduction in the biomass flux as obtained in the "wild-type" optimal solution predicted by FBA and cycleFreeFlux; and (iv) correlated reaction subsets (CRS): The flux sampling results were further used to calculate correlated reactions ($r > 0.75$) within the network. While calculating the correlations, we removed reactions with zero fluxes across the 100,000 samples. Representing the correlation matrix as an undirected graph (removing reactions with no association to other reactions) with reactions as nodes and relationship between a pair of reactions as an edge, reaction subsets (clusters) were identified using the Leiden algorithm implemented in Gephi v.0.9.2. The scaled clustering coefficient was calculated for every reaction in the graph. A reaction with a high clustering capacity (clustering coefficient > 0.75) was considered to be essential.

QUANTIFICATION AND STATISTICAL ANALYSIS

RNAscope data are from representative paraffin sections of n = 3 CNV-induced murine eyes. *In vitro* and *in vivo* functional tests were performed using at least 3 independent biological repeats as specified in the respective legends, and were analyzed by researchers blinded for the experimental condition. No statistical method was used to predetermine sample or group size. No strategy for randomization or stratification was needed, no method was used to determine whether the data met assumptions of the statistical approach. Spearman correlation and two-sided statistical significance were calculated in GraphPad Prism8. A p value < 0.05 was considered significant. A t test was used for all pairwise comparisons, ANOVA with the appropriate posthoc test for multiple group comparisons.

DATA AND CODE AVAILABILITY

Data Resources

All raw sequencing data of choroidal ECs are available in ArrayExpress under accession numbers ArrayExpress: E-MTAB-8119 (scRNA-seq data) and ArrayExpress: E-MTAB-8604 (bulk RNA-seq of ALDH18a1 and SQLE-silenced human endothelial cells). The mass spectrometry proteomics data have been deposited to the ProteomeXchange Consortium via the PRIDE (Perez-Riverol et al., 2019) partner repository with the dataset identifier PRIDE: PXD016678. Publicly available single cell transcriptome data from murine lung TECs were derived from ArrayExpress: E-MTAB-7458 and from human cultured TECs from ArrayExpress: E-MTAB-6308. Processed publicly available endothelial transcriptomics data were derived from the EndoDB, raw data can be obtained from GEO (accession number GEO: GSE77199) or ArrayExpress (accession numbers ArrayExpress: E-GEOD-41614, E-GEOD-51401, E-GEOD-73753, E-MTAB-4842). To ensure data accessibility to non-bioinformaticians, reproducibility, and resource value, we made our scRNA-seq data available for further exploration via an interactive web tool at https://www.vibcancer.be/software-tools/Murine_ECTax and the EndoDB (https://www.vibcancer.be/software-tools/endodb). With this tool users can interactively visualize gene expression and clustering on t-SNE, search marker genes for all subclusters, and export gene expression data. A database of cell cycle data is freely available at https://www.vibcancer.be/software-tools/scCycle.

Software

All software is freely or commercially available and is listed in the STAR Methods description and Key Resources Table.